A type I interferon response defines a conserved microglial state required for effective phagocytosis

Authors: Leah C. Dorman[1,2,11#], Phi T. Nguyen[1,3,12#], Caroline C. Escoubas[1], Ilia D. Vainchtein[1], Yinghong Xiao[4], Peter V. Lidsky[4], Ellen Y. Wang[1,5], Sunrae E. Taloma[1], Hiromi Nakao-Inoue[1], Brianna M. Rivera[6], Carlo Condello[6], Raul Andino[4], Tomasz J. Nowakowski[1,7,8,9,10], Anna V. Molofsky[1,7,9]*

Affiliations:
[1]Departments of Psychiatry and Behavioral Sciences/ Weill Institute for Neurosciences, [2]Neuroscience Graduate Program, [3]Biomedical Sciences Graduate Program, [4]Department of Microbiology and Immunology, [5]UCSF SRTP program, [6]Institute for Neurodegenerative Diseases/Weill Institute for Neurosciences, [7]Kavli Institute for Fundamental Neuroscience, [8]Department of Anatomy, [9]Eli and Edythe Broad Center for Regeneration Medicine and Stem Cell Research.

[1-9]University of California, San Francisco, San Francisco, CA.
[10]Chan-Zuckerberg Biohub, San Francisco, CA.

[#]These authors contributed equally.

[11]Twitter: @sculptorofdance
[12]Twitter: @Phi_hD

*Correspondence to:

Anna V Molofsky MD PhD, University of California San Francisco, 1550 4th Street, San Francisco, CA 94158, USA. Tel: 1 (415) 502-3609. anna.molofsky@ucsf.edu, @AnnaMolofskyLab

Summary

Microglia, the innate immune cells of the brain, are exquisitely sensitive to dynamic changes in the brain environment. We used single cell RNA sequencing to define glial responses in the early postnatal somatosensory cortex after partial whisker lesion, revealing transcriptomic shifts in both astrocytes and microglia during the resulting topographic remapping. The most distinct change was the emergence of a type I interferon (IFN-I) responsive microglia population that was rare in the resting cortex but expanded 20-fold after whisker deprivation. The top gene candidate in this cluster, *Ifitm3*, marked a conserved but transient subset of microglia that were in the process of phagocytosing whole cells. IFITM3 protein identified this subset in vivo, where it was enriched in early microglial phagosomes. Loss of canonical IFN-I signaling in *Ifnar1*$^{-/-}$ animals resulted in abnormal 'bubble' microglia with deficient phagolysosomal processing. In a meta-analysis of transcriptomes, we identified the IFN-I signature in microglia across a range of pathologies. We identified phagocytic IFITM3+ microglia in two murine disease models: SARS-CoV-2 infection and Alzheimer's Disease. These data reveal the potential of transcriptional profiling after defined perturbation to elicit transient microglial states, and identify a novel role for IFN-I signaling in regulating microglial phagocytosis.

Introduction

Neural circuits undergo dynamic and experience dependent changes in circuit connectivity during brain development, and even subtle alterations in this process are associated with neurodevelopmental diseases[1–4]. Glial cells, including astrocytes and microglia, are essential to physiologic neural circuit development and function[5,6]. Microglia in particular are of emerging interest due to their roles in circuit development, including promoting synapse elimination, driving synapse formation, and engulfing whole cells[7,8]. Yet despite this clear evidence of functional heterogeneity, defining the links between gene expression and function remains an active area of investigation[9,10]. One potential reason why these connections are still not completely defined is that glial heterogeneity can be transient, context-dependent, and difficult to capture. For example, while microglia broadly belong to a PU.1-dependent myeloid lineage, much of what distinguishes subsets of microglia from each other depends on dynamic responses to local factors, including cytokines, neuronal activity, and damage-associated molecular patterns[5,11–14]. Thus, defining how CNS contextual cues alter glial states is critical to linking genes to function, particularly for physiologic responses that are continuously fine-tuned to maintain homeostasis[15].

In this study, we challenged the developing murine somatosensory system with altered sensory input in order to elicit glial responses to an acute but non-inflammatory re-ordering of the neural environment. We cauterized a subset of whisker follicles in the early postnatal period to induce topographic remapping of their corresponding 'barrels' in the somatosensory cortex[16–18]. Single-cell sequencing of cortical microglia revealed marked transcriptomic shifts during remapping (https://www.annamolofskylab.org/microglia-sequencing). Most notable was a 20-fold expansion of a type I interferon (IFN-I) responsive microglial population. We identified this population *in vivo* by immunostaining for IFITM3, the top gene candidate upregulated by this cluster. IFITM3 staining revealed a rare microglial subset that expanded after deprivation and was found engulfing whole cells, with marked enrichment of IFITM3 protein at the site of nascent phagocytic cups. Disruption of IFN-I responses via deletion of the *Ifnar1* receptor resulted in dysmorphic 'bubble' microglia with excess phagolysosomes[19]. An IFITM3+ microglial subset was also widespread in a murine SARS-CoV-2 model of neurotropic viral infection, where the IFN-I responsive microglia were found neighboring infected neurons. IFITM3+ microglia also preferentially contacted and engulfed amyloid plaques in a 5xFAD model of Alzheimer's disease. Our data reveal the dynamic nature of microglial responses to homeostatic perturbations during development and identify a conserved interferon-responsive transitional state that is required for active cellular engulfment.

Results

Microglia and astrocytes alter their transcriptomes in response to cortical remapping

To elicit glial phenotypes in response to homeostatic changes in local circuits, we adapted a well-established barrel cortex remodeling paradigm. Facial whisker lesion before postnatal day 4 (P4) leads to irreversible structural alterations of the cortical topographic map, whereby synapse and cell-rich regions (barrels) separated by septa rearrange around the new sensory input space[16,18,20]. These changes lead to changes in thalamocortical input and synapse rearrangement[21–24]. Importantly, because the whisker somatosensory circuit synapses in the brainstem and the thalamus en route to the cortex, whisker lesioning leads to circuit remodeling without inducing inflammatory or injury responses in the cortex (**Fig. 1a**). This paradigm captures astrocytes and microglia during a period of active proliferation and maturation. Cortical astrocytes are present by P0, but proliferate and elaborate their processes between P0-P30[25], while microglia populate the barrel cortex septa between P3 and P5 with full invasion of the barrel centers by P7[26]. Microglia engulf barrel cortex synapses in response to complete whisker ablation[27], suggesting that this paradigm may be useful for studying microglial phagocytic responses.

Figure 1: Microglia and astrocytes alter their transcriptomes in response to cortical remapping.

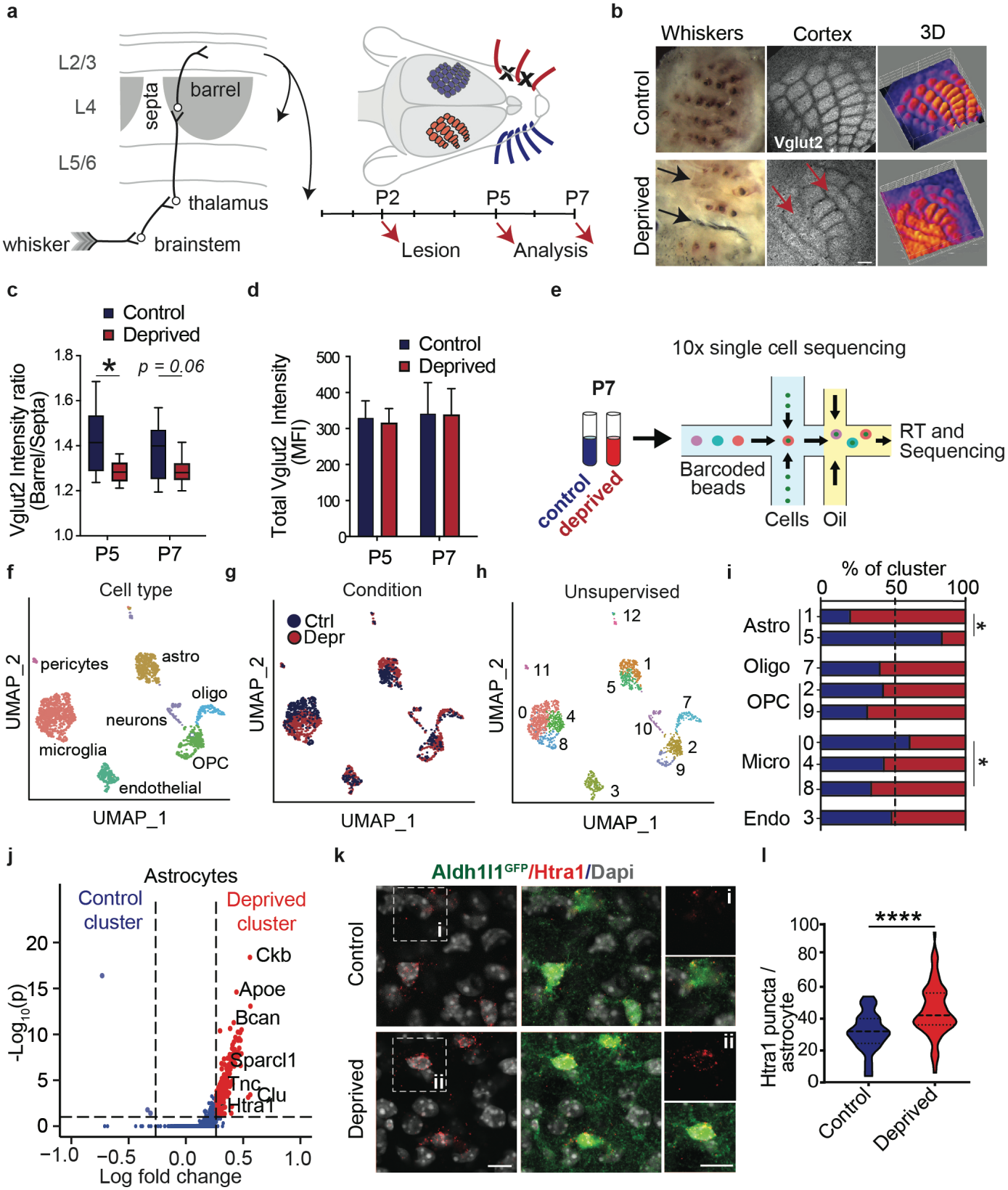

a) Schematic of barrel cortex connectivity and experimental timeline.

b) Representative images of control and whisker lesioned whisker pad (Left), *en face* imaging of L4 somatosensory cortex and cortex topographical heat map derived from VGLUT2 intensity data (right). (Scale bar = 100 μm).

c) Quantification of barrel distinctness based on VGLUT2 intensity in barrels vs. septa in control and deprived hemispheres. Box and whisker plots show range (whiskers), median, and first and third quartiles (box). (P5: n=3, P7: n=4, 2-way ANOVA with Holm-Sidak's multiple comparison test, *p<0.05).

d) VGLUT2 intensity averaged over the entire barrel field in the deprived and spared hemispheres. Error bars show mean ± SD. (P5: n=3 mice, P7: n=4, 2-way ANOVA with multiple comparisons, p>0.5).
e) Schematic of single cell barcoding and RNA sequencing using the 10x Chromium system.
f) UMAP plot of non-neuronal single cell sequencing in P7 barrel cortex labelled by cell type assigned by representative marker analysis.
g-h) Data in F plotted as control vs. whisker deprived hemisphere (**g**) and unsupervised clustering (**h**).
i) Percent of each cluster in control (blue) vs. deprived (red) hemispheres. (Chi-square test, * $p<0.01$, $f > 0.15$).
j) Differentially expressed genes between the astrocyte cluster 1 (deprived-enriched) and astrocyte cluster 5 (control-enriched.) Significance: enriched > 30%, adjusted p-value < 0.001.
k) Representative image of quantitative in situ hybridization for *Htra1* mRNA co-stained with Aldh1L1-GFP astrocyte reporter. Inset highlights a single astrocyte. (Scale bar = 10 μm)
l) *Htra1* mRNA puncta per astrocyte in control and deprived hemispheres. (n= 65 astrocytes (control) and 82 astrocytes (deprived) from n=3 mice, two-tailed t-test, ****$p< 0.0001$).
See also Figures S1-S3, Supplementary Tables 1-2

In order to elicit rearrangement but not elimination of the whisker map, we unilaterally cauterized 2/5 of the facial whiskers by removing follicles in alternating rows (B and D) at P2. We examined responses at P5 and P7, following layer 4 barrel coalescence at ~P3-P5 (**Fig. 1a**; [28,29]). For this and all subsequent experiments, we compared contralateral deprived barrel cortex with ipsilateral spared cortex as an internal control. As expected, neonatal whisker removal led to redistribution of the VGLUT2+ thalamocortical axonal boutons in cortical layer 4, whereby the deprived cortical rows (B and D) were smaller with indistinct barrel separation (**Fig. 1b,** [17]). This was reflected as a decreased ratio of VGLUT2 intensity between barrels and septa in layer 4 (**Fig. 1c**). However, mean VGLUT2 intensity across the entire barrel cortex was not significantly different, suggesting that despite redistribution, overall thalamocortical synapse density was preserved (**Fig. 1d, Fig. S1a**). Microglial and astrocyte density were unchanged (**Fig. S1b-d**), and we did not detect any evidence of astrocyte or microglial activation as measured by GFAP and Iba1 intensity respectively (**Fig. S1e-h**). We conclude that this model leads to a reorganization of the structure of the barrel cortex without provoking gross changes in synapse numbers or glial reactivity.

To define the glial response to this topographic remodeling at higher resolution, we performed single cell RNA sequencing of non-neuronal cells in microdissected somatosensory cortex. We used cold protease digestion at 4°C[30] to dissociate the tissue, which preserved most non-neuronal subsets while substantially minimizing induction of reactive markers in microglia compared to papain digestion at 34°C (**Fig. S2a-c**). Fluorescence-activated cell sorting (FACS) was used to recover live cells and enrich microglia ($CD11b^{+}/CD45^{lo}$) to 30% of total cells before single cell sequencing on the 10x Chromium V2 platform (**Fig. 1e, S2d-g**). After quality control (**Fig. S2h-j**), unbiased clustering revealed clusters specific to astrocytes, microglia, oligodendrocyte lineage cells, endothelial cells, and pericytes, whereas neurons were largely depleted (n= 1,777 cells from 2 biological replicates; **Fig. 1f-h, Fig. S1k, Supp. Table 1**). We did not detect robust changes in cell numbers, except for an increase in oligodendrocyte progenitor cells (OPC; **Fig. S3a-b**), as reported previously[31].

Notably, both astrocytes and microglia – but not endothelial or oligodendrocyte lineage cells – showed significant transcriptomic shifts following whisker deprivation (**Fig. 1i**). The astrocytes split into two clusters, one of which (cluster 5) consisted mainly of cells from the control hemisphere, while the other (cluster 1) consisted primarily of deprived cortex. Subclustering and differential gene expression analysis revealed deprivation-induced enrichment for astrocyte genes critical for synapse formation. These genes included *Sparcl1*, which physically stabilizes nascent synapses[32]. We also identified regulators of cholesterol biosynthesis necessary for synapse formation and glutamate homeostasis (*Cyp51* and *Hmgcs1)*[33–37], and extracellular matrix components and regulators, which contribute to barrel remodeling *(Bcan, Tnc, Htra1*)[38,39] (**Fig. 1j, Fig S3c-e, Supp. Table 2).** We used fluorescent *in situ* hybridization to validate a deprivation-induced increase in *Htra1*, a secreted serine

protease which degrades extracellular matrix (**Fig. 1k-l**;[40–43]). Microglial clustering showed a more complex response to remodeling than astrocytes, prompting us to study microglia at higher resolution in subsequent experiments.

A type I interferon-responsive microglial subset expands 20-fold during cortical remapping

Microglia have multiple developmental functions that may be relevant to barrel maturation. They engulf synapses in some developmental and disease contexts[44,45], promote synapse formation, maturation, and plasticity[26,46,47], and engulf dead or dying cells[48–51]. Neuronal cell death in this region peaks at P5-P6 and ongoing synaptic and dendritic formation and remodeling occurs throughout the first postnatal week and beyond[18,52]. In order to molecularly define this microglial response with additional temporal resolution, we performed single cell RNA sequencing of microglia at P5 and P7 after induction of topographic remapping via whisker removal at P2. We purified microglia using mechanical dissociation followed by magnetic bead isolation, which is ideal for preserving *in vivo* microglia signatures, although it depletes other glial subsets (**Fig. 2a**,[53–57]). We recovered 12,330 cells from 10 mice after quality control and identified 8 microglial clusters, 4 of which were altered by whisker deprivation (**Fig. 2b-e, Fig. S4a-d, Supp. Tables 3-4**). Cell cycle analysis showed that clusters 1, 2, and 6 clustered mainly by markers of the different stages of cell division and thus were not examined further (**Fig. S4e-f**). These proliferating clusters were more abundant at P7 than P5 (**Fig. S4g-h**). We also identified a small macrophage subset (1% of cells, cluster 9, *Pf4*, *Lyve1*) that was not substantially changed by whisker deprivation. We focused on the four non-proliferative clusters of microglia (0,3,4,8), which all changed in relative abundance after cortical remodeling. Cluster 0, the largest subset, was most similar to a homeostatic microglial cluster (*P2ry12, Ccr5*), and decreased modestly after whisker deprivation. Adjacent to this, cluster 4 was decreased after whisker deprivation. In contrast, cluster 3 was distinct in UMAP space, and significantly increased after whisker deprivation (**Fig. 2c-d**).

The most striking difference between control and whisker-deprived conditions was the emergence of a microglial subpopulation enriched in type I interferon (IFN-I) response genes (cluster 8). The IFN-I response is a highly evolutionarily conserved antiviral response, but its functions in the developing brain are unknown[58]. Differential gene expression and Gene Ontology (GO) analysis on cluster 8 revealed a robust interferon response signature (*Ifitm3*, *Mx1*, *Ifit3, Isg15*, *Irf7,* and *Stat1)* and GO terms "Response to virus" (GO:0009615), "Response to interferon-alpha" (GO:0035455), and "Response to interferon-beta" (GO:0035458) (**Fig. 2f-g**). This cluster was located between microglia and macrophages in UMAP space but showed microglia-like expression of *Tmem119*, *Tgfbr1*, and *Hexb* (**Fig. S4i**). The interferon-responsive cluster 8 was enriched 20-fold in P5 deprived vs. control cortices (0.5% in control vs 11% in deprived) but was indistinguishable from control by P7 (0.6% vs 0.4%) (**Fig. 2h-i, Fig. S4j-m**). These data reveal a novel microglial subset that is rare in the typically developing cortex, but expands markedly during a restricted phase of topographic remapping.

Interferon-responsive microglia transition towards a cell-engulfing microglial state

To predict the directionality of molecular changes and the dynamic relationships between interferon-responsive cluster 8 and its neighbors, we performed RNA velocity analysis. Velocity analysis takes advantage of the ratio of unspliced pre-mRNA to spliced mRNA to infer trajectories between neighboring clusters on the time scale of hours, with higher velocities predicting a faster transition between cell states[59]. Interferon-responsive cluster 8 showed a predicted trajectory towards cluster 3 (**Fig. 3a)**, a cluster which also expanded during topographic remapping (**Fig. 2d**). Of note, clusters 3 and 8 were both distinct from the predominant cluster enriched for GO terms and genes linked to lysosomal function, cluster 4 (*Cd68, Trem2, Apoe*; GO:0005764, "lysosome"). Cluster

4 in turn was the most similar to 'proliferative-region associated microglia' (PAMs, 38/42 genes upregulated;[9,10]) and was the only cluster to exhibit modest similarity with 'damage-associated microglia' (DAMS,[60]) identified in previous studies (36/83 genes upregulated; **Fig. S4n-o**). From this, we conclude that the interferon-responsive cluster 8 is a unique microglial subset that may be a precursor population to the larger cluster 3.

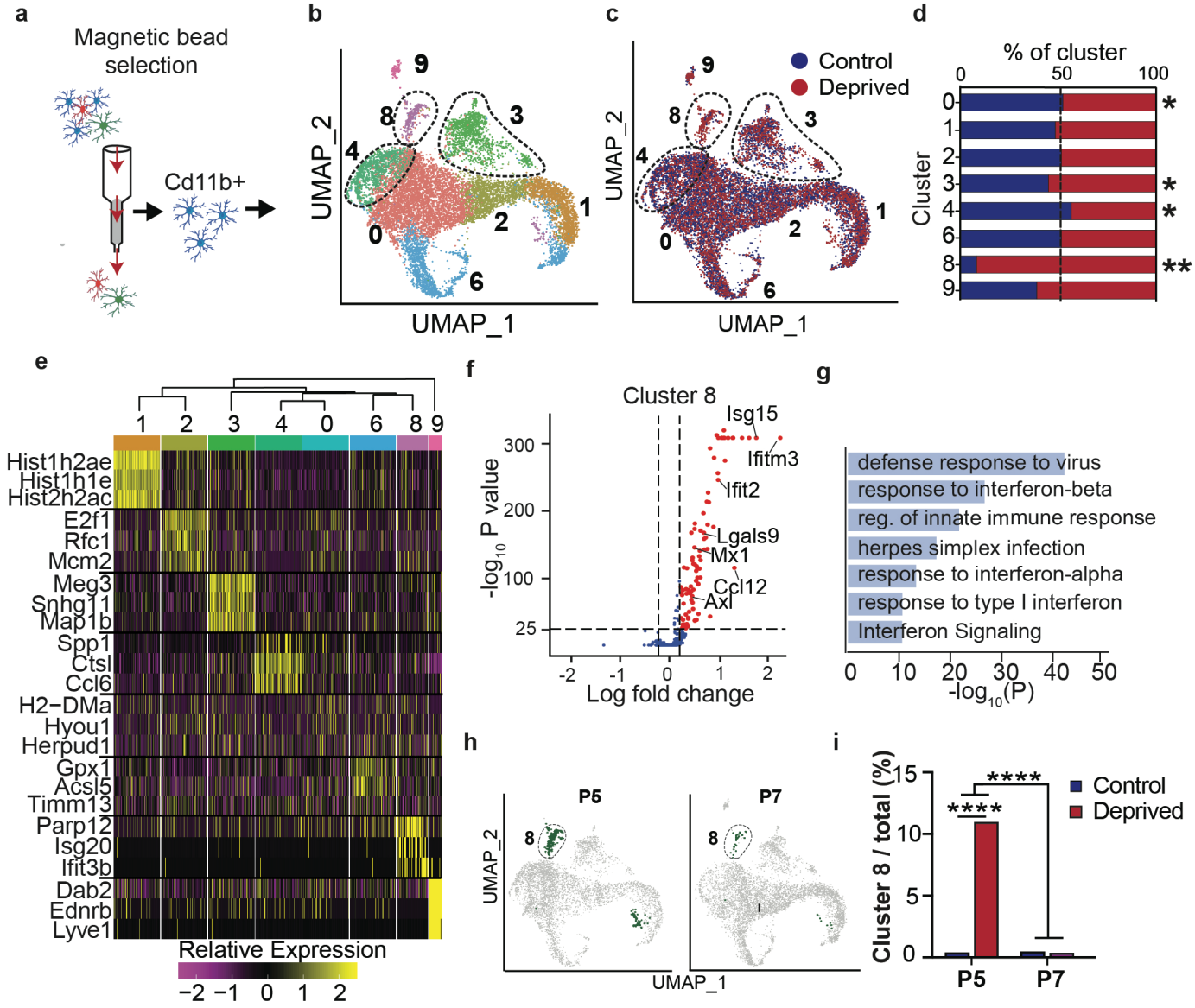

Figure 2. A type I interferon-responsive microglial subset expands 20-fold during cortical remapping.

a) Schematic of MACS-isolation of microglia for single cell sequencing.

b) UMAP plot showing independent clustering of 12,000 CD11b+ cells, pooling P5 and P7 timepoints from control and whisker deprived cortices, including microglia (Clusters 0- 8) and macrophages (Cluster 9). Dotted lines highlight clusters for further analysis.

c) Clusters colored by condition (control vs. whisker deprived).

d) Quantification of cluster composition by condition. X-axis represents percent of cells in each cluster from the control (blue) or deprived (red) hemispheres, normalized for total number of cells per sample. (Chi-square test with Bonferroni correction, * p_{Adj} <0.01, ** $p_{Adj} < 10^{-25}$).

e (log_2 fold change, $p_{Adj} < 10^{-25}$).

f) Volcano plot of genes differentially expressed in cluster 8 relative to all other clusters.

g) Cluster 8 upregulated GO terms.

h) Clusters separated by age (P5 vs. P7) with cluster 8 highlighted (green).

i) Plot of cluster 8 abundance at each time point in control vs. deprived conditions (Chi-square test with Bonferroni correction, **** $p_{Adj} <10^{-10}$).

See also Figure S4, Supplementary Tables 3-4

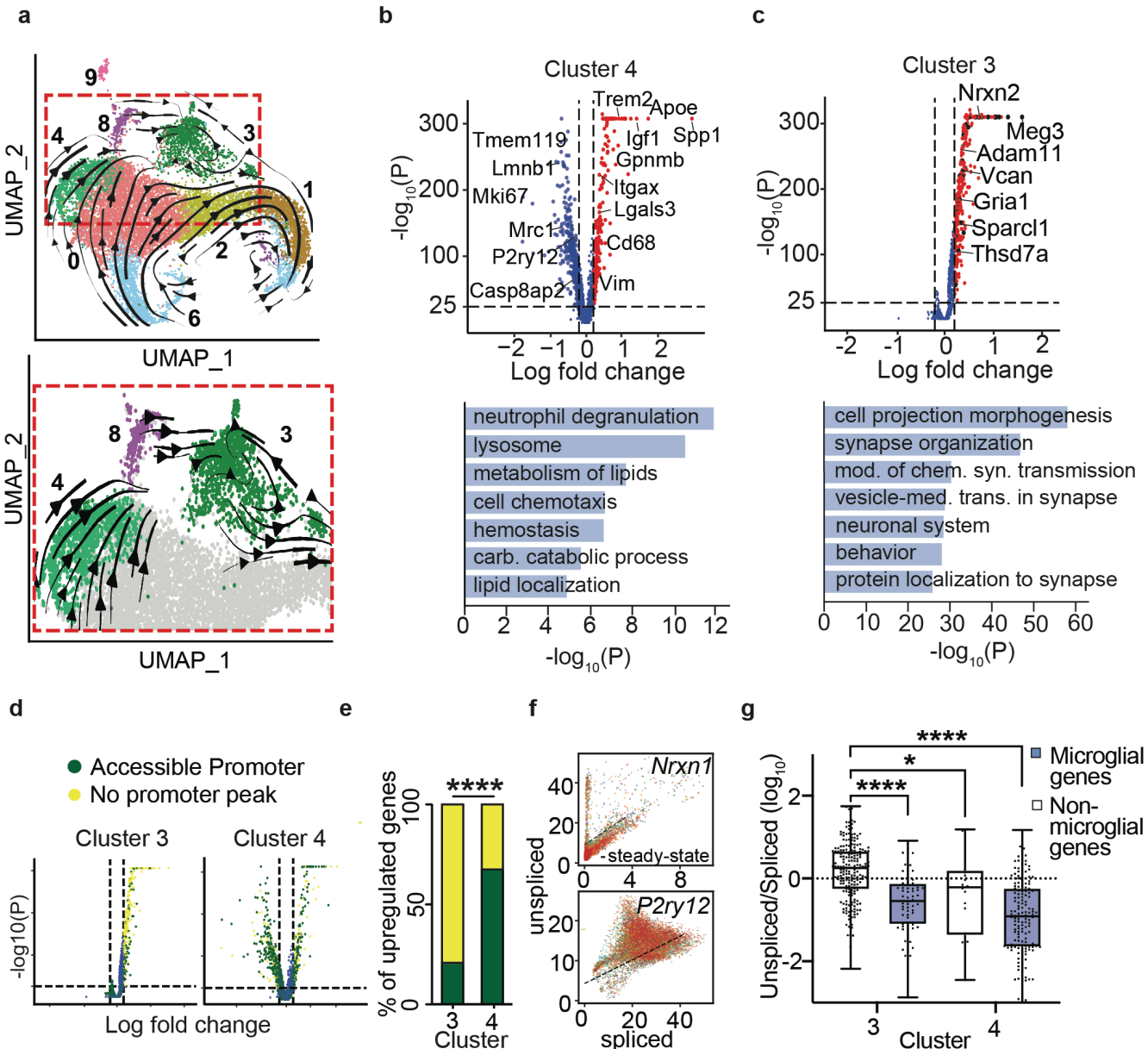

Figure 3. Interferon-responsive microglia transition towards a cell-engulfing microglial state.

a) RNA velocity analysis colored by cluster (scVelo, [59]); Inset (below) highlights clusters 3, 4, and 8.

b-c) Differentially expressed genes and upregulated GO terms for Cluster 4 (**b**) and Cluster 3 (**c**).

d) Volcano plots in **c** and **b**, colored by genes with accessible promoters (green) vs. no promoter peak (gray) from ATAC-seq data from P30 somatosensory cortex microglia. "Accessible promoter" defined as ATAC-seq reads > 10th percentile of all peaks, "no promoter peak" defined as reads below 10% threshold.

e) Volcano plot of differentially expressed genes with accessible promoters vs. no promoter peak in clusters 3 and 4 (Chi-Square test).

f) Representative plots of transcript status for a canonical neuronal gene (*Nrxn1*) vs. a microglial gene (*P2ry12*). Each dot represents one cell; units are in transcript counts per cell.

g) Ratio of unspliced:spliced transcripts (log_{10}) for enriched genes in clusters 3 and 4, for canonical microglial genes (blue) vs. genes enriched in other cell types (white). "Enriched" = 10x higher FPKM in microglia than the mean of other cell types from [61]. Box and whisker plots show data range, median, and first to third quartiles. (One-way ANOVA with Dunnett's multiple comparisons).

Statistics: Thresholds in **a, b, c, d, e, g** are $p_{adj} < 10^{-25}$ >, natural log fold change > 0.2. *p<0.05, **p<0.01, ****p<0.0001.

See also Supplementary Tables 5-6

To explore the potential functional relationship between the IFN-I responsive cluster and its predicted future cell state, we examined cluster 3 in further detail. Differential gene expression and ontology showed a marked enrichment in mRNAs associated with other cell types, including neurons (*Map1b, Nrxn2, Gria1*), oligodendrocytes *(Vcan*), and astrocytes (*Sparcl1*), without any downregulation of canonical microglial genes

(**Fig. 3c**). Non-microglial mRNA could indicate an atypical gene expression profile, or it could result from phagocytosed foreign material. Although we cannot rule out the former possibility, we concluded that it was unlikely for two reasons. First, the promoters for these genes were significantly less likely to be accessible relative to promoters of known microglial genes expressed by cluster 4 based on cross-correlation with an ATAC-Seq dataset of cortical microglia (**Fig. 3d-e, Supp. Table 5**). Secondly, these non-canonical microglial genes in cluster 3 were significantly enriched for intronic sequences associated with unspliced transcripts, relative to canonical microglial genes (**Fig. 3f-g, Supp. Table 6**). Interestingly, cluster 3 microglia strongly upregulated the phosphatidylserine receptor (*Adgrb1,* BAI1) as well as the TAM receptor *Axl*, suggesting that these microglia may be preferentially primed for engulfment of cells or synapses[49,62–66]. We therefore hypothesized that these foreign RNA containing microglia (cluster 3) represent a microglial subset that is in the process of engulfing whole cells, thereby capturing nuclear material and pre-mRNA from other cell types. Together with the finding that interferon-responsive cluster 8 decreased ~20-fold from P5 to P7 (**Fig. 2h-i**), we hypothesized that cluster 8 was a transient intermediate state that emerged prior to cell engulfment.

The transmembrane protein IFITM3 defines a phagocytic microglial subset enriched during cortical remapping

To further determine whether interferon-responsive microglia represented a *bona fide* microglial subtype *in vivo*, we identified markers that could be used for immunostaining in tissue sections. *Ifitm3* was the most highly upregulated gene in interferon-responsive cluster 8 (**Fig. 2f, Fig. 4a**). This IFN-α/β - stimulated gene encodes a transmembrane protein with pleiotropic roles in limiting viral replication, cancer progression, and amyloid beta plaque deposition[67–70]. We identified a rare population of IFITM3+ microglia in developing barrel cortex that were found primarily in layers 4 and 5 and were increased up to 8-fold during topographic remapping, as quantified *in situ* and by flow cytometry **(Fig. 4b-c; Fig. S5a-d).** We further confirmed that IFITM3+ cells expressed *Mx1*, the canonical interferon stimulated transcription factor also upregulated by cluster 8, as assessed by flow cytometry using an $Mx1^{GFP}$ reporter[71] (**Fig. S5e-f**). Based on the similarities in developmental abundance, induction with barrel remodeling, location near barrels, and expression of two different markers that define our single cell cluster, we conclude that IFITM3 can be used to identify the interferon-responsive cluster 8 *in situ*.

We observed that IFITM3+ microglia were morphologically unique, with at least two distinct morphological subtypes. One type exclusive to layer 4, which we called 'barrel invading', extended a singular primary process deep into the barrel hollow at P5, a time period when microglia are in the process of colonizing barrel centers [26]. A second type contained prominent IFITM3 enriched phagocytic cups enveloping DAPI+ nuclei (**Fig. 4d-e**). In contrast, IFITM3- microglia were predominantly ramified with a homeostatic morphology. IFITM3+ microglia were also more likely to contain multiple DAPI-containing phagosomes, which appeared only rarely in IFITM3- microglia (**Fig. 4f-g**). These data suggest that IFITM3+ cells are more likely to be engulfing cellular material, and that IFITM3 may be involved in the process of phagocytosis based on its enrichment in the phagocytic cup.

Given that phagocytosis is an essential microglial function, we wondered if this interferon response signature was unique to whisker deprivation or possibly a more common but short-lived microglial state. To examine this *in situ*, we fate-mapped interferon-responsive cells using $Mx1^{Cre}$ mice (Jax 003556) crossed to a tdTomato reporter line (*Ai14;* Jax 007908) in order to identify cells that express the cluster 8 marker and canonical IFN-I response gene *Mx1* during their life cycle[72]. We found that approximately 20% of microglia in control cortices at P7 were $Mx1^{TdT}$+ (vs. 1% IFITM3+ cells at P5). This increased to ~50% after deprivation (vs. 12% IFITM3+; **Fig. 4h-i**). These data suggest that many cells not expressing IFITM3 were interferon-responsive at some point in their lifetime. Together with our transcriptomic results predicting that IFN-I responsive microglia move towards a cell

engulfing state, we hypothesized that the IFN-I response is a transient state in the microglial phagocytic cycle that could play a critical but underappreciated role in phagocytosis.

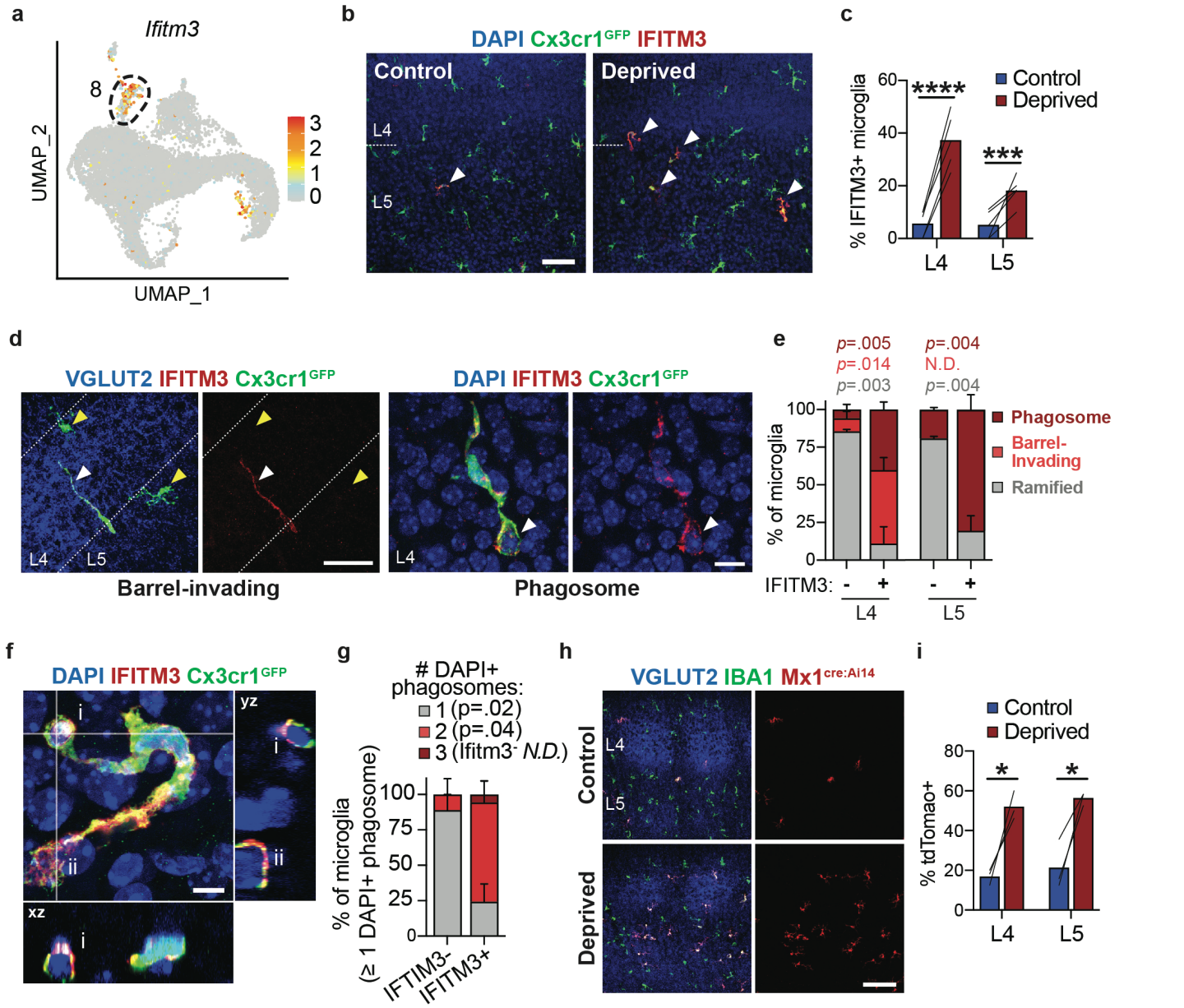

Figure 4. The transmembrane protein IFITM3 defines a phagocytic microglial subset enriched during topographic remapping.

a) UMAP feature plot showing normalized expression of cluster 8 marker gene *Ifitm3*.
b) Representative image of IFITM3+ microglia (arrowheads) in whisker-deprived somatosensory cortex at P5 (Scale bar = 50 μm).
c) Percent IFITM3+ microglia in coronal sections from layers 4 and 5 (L4, L5). Lines connect control and deprived from the same mouse (n=5, Two-way Repeated Measures (RM) ANOVA with Sidak's Multiple Comparisons. *** p< 0.001, ****p<0.0001)
d) Representative image of 'barrel-invading' IFITM3+ microglia and 'phagosome-containing' IFITM3+ microglia in P5 deprived cortex (Coronal sections, scale bar = 20 μm (left), 5 μm, (right))
e) Quantification of microglial morphological subtypes described in **e** (n = 4 mice, paired t-test).
f) Confocal image and orthogonal views of an IFITM3+ microglia containing multiple phagosomes (i, ii show nuclei-containing phagosomes that are distinct from the microglia nucleus). (Scale bar = 5 μm)
g) Number of phagosomes per microglia, among microglia with at least one DAPI+ phagosome (n = 4 mice, paired t-test).
h) Representative images of tdTomato+ cells (*Mx1-Cre;Rosa26-LSL-TdT*) in layers 4-5 of barrel cortex co-labeled with microglial marker IBA1 and VGLUT2 to highlight barrels.
i) TdTomato+ microglia in control and deprived sections. (n = 3, paired two-tailed t-test, * p< 0.05).
Data are mean ± SEM (stacked bar graphs). ***See also Figure S5.***

IFITM3 is a marker of early microglial phagosomes

We noticed an enrichment of IFITM3 around phagocytic cups (**Fig. 4f**), prompting us to further examine the relationship between IFITM3 and the phagocytic cycle. We observed that IFITM3+ cells had higher lysosomal content than their IFITM3- counterparts as measured by percent CD68+ volume, consistent with increased phagocytic capacity (**Fig. 5a-b**). Phagocytosis proceeds in stages, including membrane remodeling and enveloping of extracellular material, packaging into a phagosome, and fusion to mature lysosomes to form a phagolysosome[73]. Therefore, we more closely examined distinct stages of the phagosome to better define the potential role of interferon signaling and IFITM3. We observed both early phagosomes, which we defined as a $CD68^{low}$ microglial process partially enveloping a non-pyknotic DAPI+ nucleus, and late phagolysosomes that were $CD68^{high}$ and fully surrounded dense DAPI+ inclusions (**Fig. 5c**,[74]). While IFITM3+ cells had more lysosomes overall, we observed that they were also much more likely to have early phagosomes; 90% of IFITM3+ microglia had at least one early phagosome, compared to 7% of IFITM3- microglia **(Fig. 5d**). In IFITM3+ phagosome-containing microglia, a majority contained both early and late phagosomes in the same cell, a phenomenon not observed in IFITM3- microglia (**Fig 5e, Fig. S5g).** We also examined the morphologies of individual phagosomes in IFITM3+ microglia and tracked their progress from an early incomplete phagocytic cup to a mature CD68+ phagolysosome (**Fig. 5f**). We found a significant inverse correlation between IFITM3 and CD68 (**Fig. 5g**), suggesting that IFITM3 is expressed in the early stages of phagocytosis. Finally, we found that whisker deprivation led to a significant increase in the number of microglia with phagosomes (**Fig. 5h-i)**, consistent with the increase of IFITM3+ microglia after deprivation. This data suggests that IFITM3 marks an early stage in microglial engulfment and phagocytosis and is particularly enriched in microglia containing multiple maturing phagosomes.

Type I interferon signaling is required for microglial phagosome maturation

To determine whether IFN-I signaling is required for microglial phagocytosis, we examined mice lacking the obligate IFN-I receptor *Ifnar1* (Jax 028288; **Fig. 6a**). We found that *Ifnar1* was required for microglial IFITM3 expression after whisker deprivation (**Fig. 6b**), confirming that our interferon-responsive microglial subset requires canonical IFN-I signaling. We found that microglia from *Ifnar1*$^{-/-}$ mice contained significantly larger phagosomes than wild type mice (**Fig. 6c-d**). Microglial phagosomes in *Ifnar1*$^{-/-}$ mice also had a distinct morphology, with enlarged thin walls containing diffuse DAPI+ nuclear material. In contrast, wild-type microglia had smaller phagosomes with condensed DAPI signal that was completely enveloped by the membrane (**Fig. 6e**). These microglia were reminiscent of previously described 'bubble' microglia observed in zebrafish with mutations in a gene required for phago-lysosomal fusion[19]. We quantified bubble microglia, defining them as microglia with a phagosome larger than the microglial nucleus and with a dim DAPI signal. We found that bubble microglia were rare in control mice, representing 5% of microglia, and tended to increase to about 15% of microglia after partial whisker deprivation. In contrast, up to 40-60% of barrel cortex microglia from *Ifnar1*$^{-/-}$ mice had bubble morphologies (**Fig. 6f**). Additionally, we observed that microglia from IFN-I deficient animals had significantly more phagosomes (**Fig. 6g**) and frequently had multiple phagosomes per cell (**Fig. 6h-i, Supplemental movie 1).** We conclude that deficient IFN-I signaling results in abnormal microglial phagolysosome function and a buildup of phagolysosomal compartments within microglia.

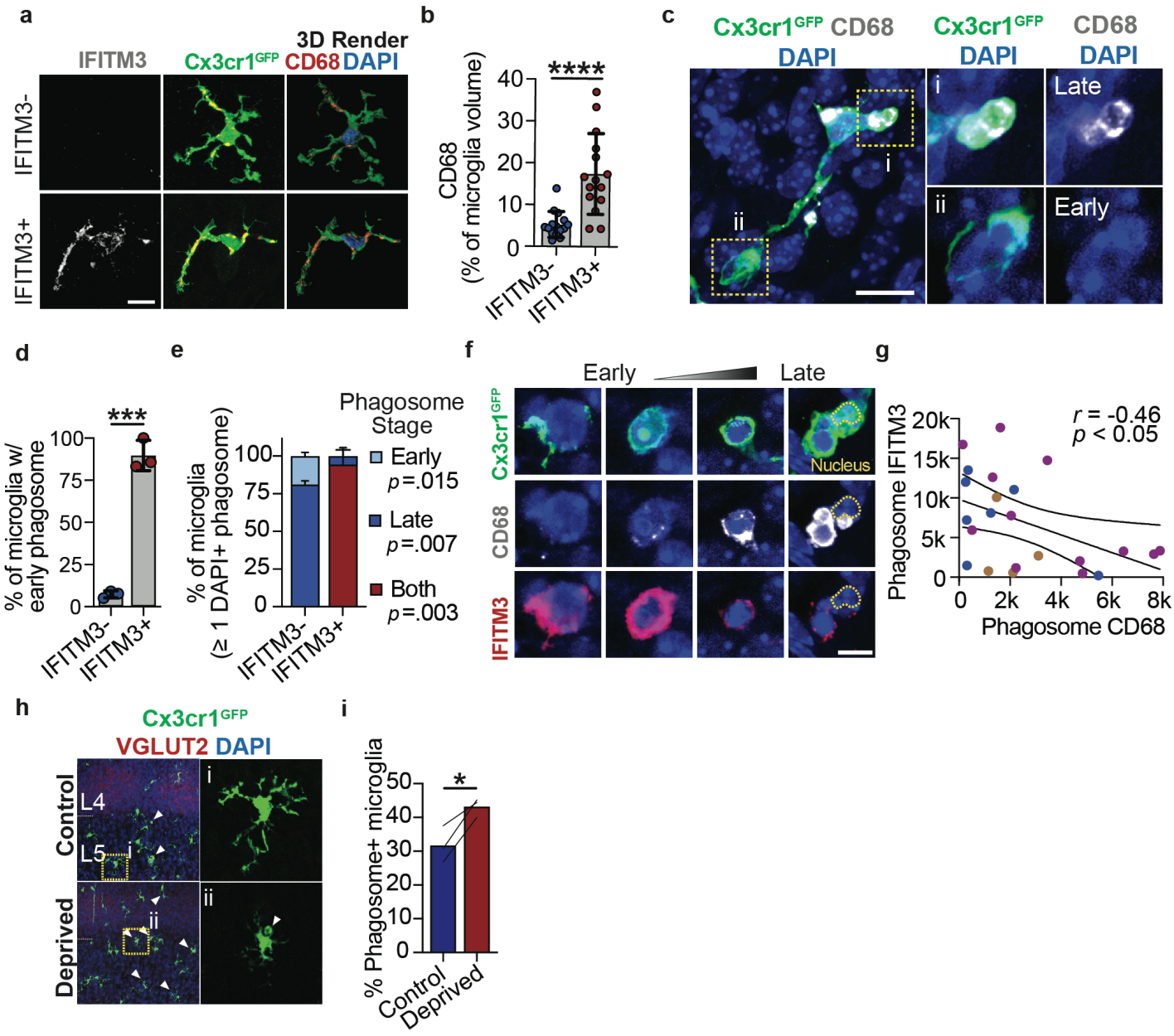

Figure 5. IFITM3 is a marker of early microglial phagosomes.

a) Representative images and 3D-rendering of CD68+ lysosomes within IFITM3+ and IFITM3- microglia in L4. (Scale bar = 10 µm)

b) Quantification of % CD68 volume of total microglial volume in IFITM3+ and IFITM3- microglia (13 IFITM3- and 15 IFITM3+ from n= 3 mice, two-tailed t-test).

c) Representative image of a Cx3cr1-GFP+ microglia highlighting a late phagosome/phagolysosome (i; $CD68^{+}$, condensed DAPI signal, complete DAPI envelopment by microglial processes) and an early phagosome (ii; $CD68^{-}$, non-pyknotic DAPI signal, incomplete envelopment by microglial processes). (Scale bar = 10 µm).

d) Percent of IFITM3- and IFITM3+ microglia containing an early phagosome. (n = 3 mice, two-tailed t-test).

e) Distribution of early and late phagosomes as a proportion, in microglia containing at least one phagosome. (n = 7-10 cells each from 3 mice/group, RM ANOVA).

f) Representative images showing changes in IFITM3 and CD68 expression with phagosome maturation. (Yellow dotted line = microglial nucleus, Scale bar = 5 µm)

g) Correlation of CD68 and IFITM3 mean fluorescence intensity per phagosome (n = 23 cells from 3 mice, Pearson correlation).

h) Representative images of microglia in control and deprived cortex, inset: single microglia (scale = 50 µm, arrowheads= phagosome).

i) Percent microglia containing at least one phagosome in control vs. deprived cortices (P5, n = 3, paired two-tailed t-test).

Statistics: * p< 0.05, *** p< 0.001, **** p< 0.0001. Data are mean ± SD (bar graphs) and mean ± SEM (stacked bar graphs).

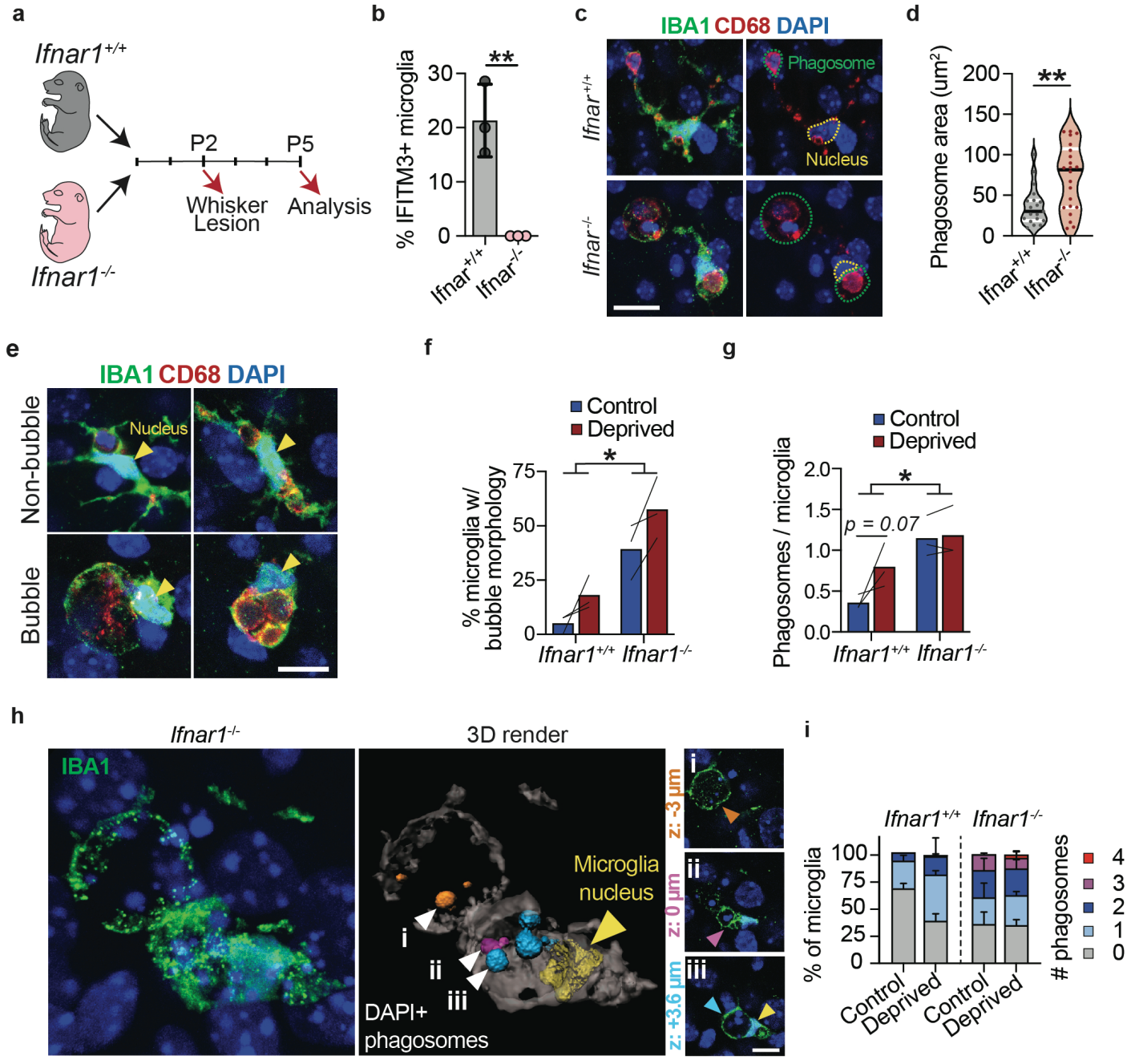

Figure 6: Type 1 interferon signaling is required for microglial phagosome maturation.

a) Diagram of experimental design comparing control (*Ifnar1*$^{+/+}$) vs. IFN-I insensitive (*Ifnar1*$^{-/-}$) mice.

b) IFITM3+ microglia in deprived hemispheres (L4-5 barrel cortex) from *Ifnar1*$^{+/+}$ and *Ifnar1*$^{-/-}$ (n = 3 mice, 2-tailed t-test, ** p<0.01).

c) Representative image of microglia from *Ifnar1*$^{+/+}$ and *Ifnar1*$^{-/-}$ mice. (yellow: microglial nucleus, green: phagosomes, Scale = 15 µm)

d) Phagosome area per microglia in barrel cortex from *Ifnar1*$^{+/+}$ and *Ifnar1*$^{-/-}$ mice. (n = 3 mice per genotype, 2-tailed t-test, ** p<0.01).

e) Representative images of "bubble" microglia with rounded phagosomes larger than the microglia nucleus (Scale = 10 µm)

f) Percent microglia with bubble phagosomes in control and deprived barrel cortices from *Ifnar1*$^{+/+}$ and *Ifnar1*$^{-/-}$ mice (n = 3 mice per genotype, RM ANOVA with Sidak's multiple comparisons, * p< 0.05).

g) Phagosomes per microglia in control and deprived cortices from *Ifnar1*$^{+/+}$ and *Ifnar1*$^{-/-}$ mice. (Lines connect control and deprived hemispheres from individual mice, n = 3 mice/ genotype, RM ANOVA with Sidak's multiple comparisons, * p< 0.05).

h) Representative image and 3D render of microglia with multiple phagosomes in *Ifnar1*$^{-/-}$ mouse (White arrowheads: DAPI+ phagosomes; Yellow: microglial nucleus). Insets: cross sections through each phagosome, colored as in render (Scale bar = 10 µm).

i) Data in **g** plotted to highlight distribution of number of phagosomes per microglia.

See also Supplemental movie 1.

Microglia upregulate a conserved interferon-response signature in pathology

To determine if interferon-responsive microglia are unique to this experimental paradigm, we examined murine microglial bulk transcriptomic datasets from a variety of physiological and pathological conditions (**Fig. 7a**, **Supp. Table 7**[75]). As expected, we found the greatest enrichment of the interferon-response signature after viral infection (lymphocytic choriomeningitis, LCMV). However, we also detected prominent induction of an interferon response in various sterile pathologies, including mouse models of brain tumors and of Alzheimer's disease (AD). Although single cell datasets are still comparatively rare, we found that the interferon-response signature was also enriched in a subset of microglia after demyelinating injury (LPC, Cuprizone treatment) and in aging brains (18 month old mice) (**Fig. S6a-b**,[9]) as well as in a model of Alzheimer's disease[75,76].

Type I interferon signaling is one of the first lines of defense against viral infection, and we expected to see IFITM3 upregulated in microglia after viral infection based on canonical signaling and transcriptomic data (**Fig 6a**,[58]). In order to examine whether IFITM3 was increased in microglia and marked a phagocytic population as we observed during development, we used a mouse model of SARS-CoV-2 infection, given its major public health interest, known involvement of IFITM3[77–79], and recent reports of potential neurologic sequelae[80–82]. We performed intranasal inoculation of a SARS-CoV-2 strain isolated from a patient into K18-ACE2 transgenic mice, which express the human ACE2 receptor under the cytokeratin-18 (K18) promoter[83–86].

In contrast to developmental remodeling, we found that most microglia in brains with active viral replication expressed high levels of IFITM3. We detected active CNS viral replication in 2 out of 3 mice at 6 days post infection (DPI) but 0 out of 3 mice at 3 DPI, as assessed by SARS-CoV-2 Spike and N-protein expression, consistent with recent reports **(Fig. S7a-d**; [87,88]). We found that infected cells were almost exclusively NeuN+ neurons, with highest infection levels in cortex and hippocampus, lower levels in the olfactory bulb, and undetectable levels in the cerebellum (**Fig. S7c-d**). Focusing on somatosensory cortex, we identified a significant increase in microglial IFITM3 immunoreactivity in infected mice at 6 DPI (**Fig. 7b-c**). IFITM3 intensity was strongly correlated with infectivity, as assessed by Spike protein intensity (r=0.93, **Fig. 7d-e**), although we detected IFITM3 both in microglia and non-microglial cells (likely astrocytes). Microglia expressing higher levels of IFITM3 were also more likely to have a phagosome engulfing SARS-CoV-2 Spike+ cells (**Fig. 7d,f, Fig. S6e**) and were more likely to have an activated morphology (**Fig. S6f**).

We then investigated whether IFITM3+ microglia could also be identified in a sterile model of neurodegeneration. Type I interferon responses have been shown to exacerbate pathology in aging and Alzheimer's disease and are associated with microglial activation[75,76,89–92]. To determine if an interferon-responsive microglial subset is present in AD mouse models *in situ*, we analyzed IFITM3 expression in brains from 12-month-old 5xFAD mice. This mouse model of Alzheimer's disease undergoes Aβ deposition and plaque formation followed by decreased performance on cognitive tasks and neuronal loss by 9 months[93]. We observed that 21% of microglia in the ventral hippocampus of 12 month old 5xFAD mice were IFITM3+, whereas few were detected in aged-matched controls (**Fig. 7g-h**). We also detected IFITM3 in astrocytes as previously described[67], which was ubiquitous throughout the hippocampus in both control and 5xFAD settings and enriched in a GFAP+ cytoskeletal pattern (**Fig. 7g**). IFITM3+ microglia were significantly more likely to be associated with amyloid plaques than IFITM3- microglia and were twice as likely to contain at least one phagocytic cup (**Fig. 7i-j**). As in the developing cortex, these phagocytic cups were enriched for IFITM3 protein (**Fig. 7g, k**). We observed a positive correlation between IFITM3 levels within phagocytic cups and the amount of engulfed Aβ (**Fig. 7k-l**). Microglial phagocytosis of Aβ is known to limit plaque deposition and neurotoxicity[94,95], suggesting that interferon-responsive microglia could play a neuroprotective role.

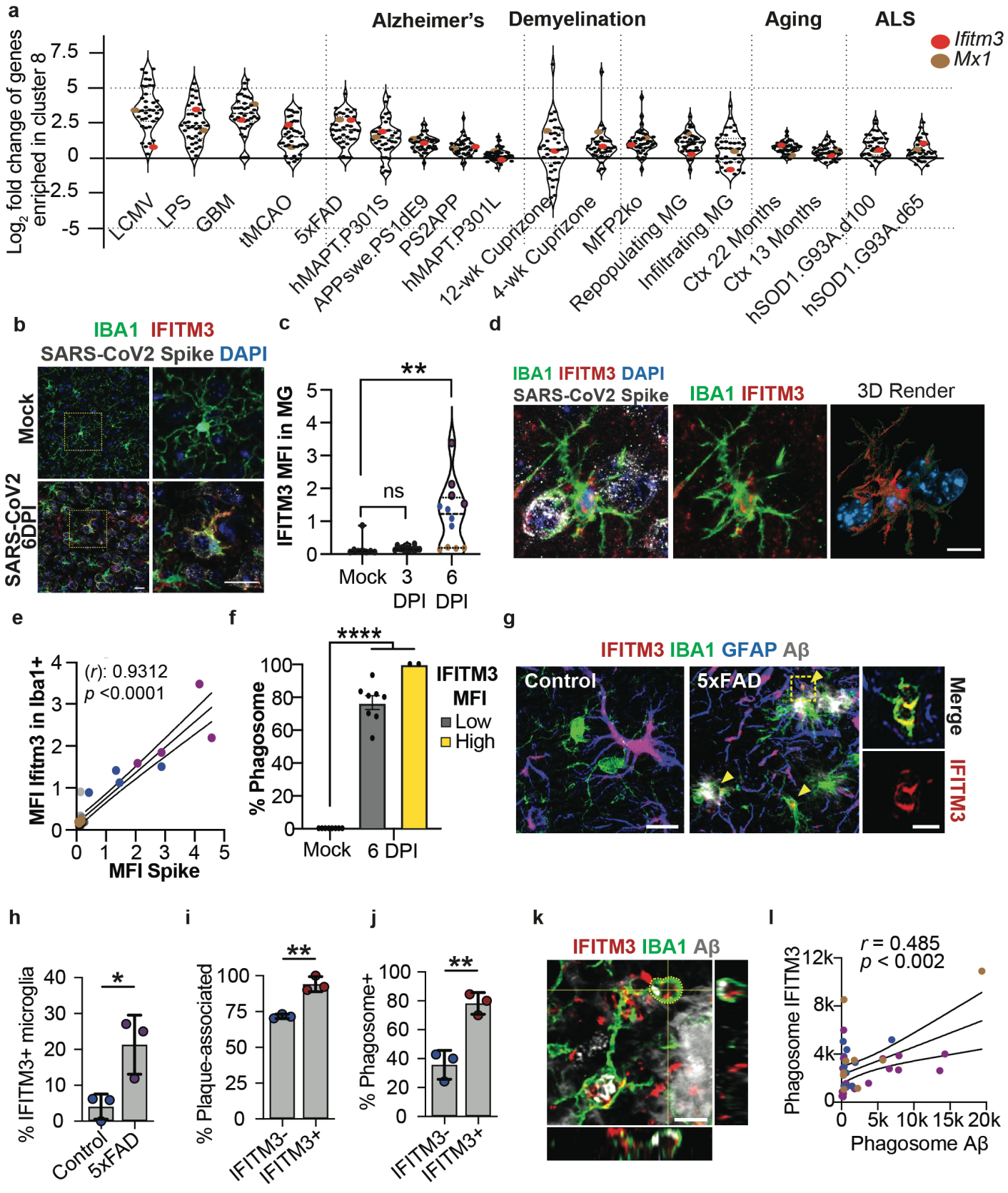

Figure 7: Microglia upregulate a conserved interferon-response signature in pathology.

a) Expression of 38 'cluster 8' marker genes across a set of published microglia sequencing data (from bulk sorted CD11b+ cells[75]. Dots represent individual genes, highlighting *Ifitm3* (red) and *Mx1* (orange). y-axis represents the log-fold-change relative to the control in that dataset. See Supplementary Table 7 for details of each sample set and experimental condition.

b) Representative images in somatosensory cortex showing IFITM3 staining in Iba1+ microglia from mock vs. SARS-CoV-2 infected mice 6 days post infection (DPI) (left: low power, right: inset, single microglia, Scale bar = 20 μm).
c) Quantification of IFITM3 mean fluorescence intensity within microglia. Each color represents an individual mouse. (n=2 mock-infected mice, 3 each at 3 and 6 days post infection, 2 way ANOVA with Sidak's multiple comparisons test, **p< 0.01).
d) Representative image and 3D reconstruction of an IFITM3+ microglia engulfing a SARS-CoV-2 infected cell. (Scale= 10 μm).
e) Correlation of SARS-CoV-2 Spike protein vs. microglial IFITM3 per field of view. Colored by mouse (n = 3 mice at 6 DPI, Pearson Correlation).
f) Percent phagosome-containing microglia in cortices of mock-infected vs. SARS-CoV-2 infected mice at 6 dpi, binned by IFITM3 expression per cell (see Methods for details). (Dots are fields of view from n = 2 mice/group, One-way ANOVA with Tukey's multiple comparisons test, ***p< 0.001).
g) Representative images of microglia in hippocampi of 12-month old 5xFAD and age matched control mice, labeled with IFITM3, microglia (IBA1), astrocyte (GFAP), and Aβ (FSB dye). Inset: the plaque-adjacent phagosome outlined in yellow.
h) Percent IFITM3+ microglia in 5xFAD and control hippocampi. (n = 3 mice per group, two-tailed t-test, * p< 0.05)
i) Percent of microglia in IFITM3+ and IFITM3- populations within 10 μm of an Aβ plaque (n = 3 mice, two-tailed t-test, **p< 0.01).
j) Percent of microglia in IFITM3+ and IFITM3- populations containing a phagosome (n = 3 mice, two-tailed t-test, ** p< 0.01).
k) Confocal image and orthogonal projection of a plaque-associated IFITM3+ microglia with an Aβ+ (4G8 antibody) IFITM3+ phagosome. (Scale bar = 5 μm).
l) Correlation of Aβ and IFITM3 mean fluorescence intensity per phagosome. (Colored per mouse, Pearson Correlation).
Statistics: * p< 0.05, ** p<0.01, *** p< 0.001, **** p< 0.0001. All error bars show mean ± SD.
See also Figures S6-S7, Supplemental Table 7.

Discussion

In this study we defined a coordinated set of functional state changes in microglia in response to developmental barrel cortex remodeling. We identified an interferon-responsive, highly phagocytic population that emerged transiently in the whisker-deprived context and was conserved in both sterile and inflammatory disease models. We also found that IFN-I signaling is required for effective microglial phagocytosis. IFN-I responses are a central component of antiviral defense, and have been linked to phagocytosis in some pathogenic contexts, but their role in physiology is comparatively unknown[96–99]. Our IFN-I responsive microglial subset is rare but detectable in the normally developing cortex, and a perturbation that altered the pattern of developmental remodeling enabled their definitive identification. In mice lacking IFN-I responses, up to 40% of microglia are highly dysmorphic with altered phagocytosis. This loss of function data argues that IFN-I microglia are rare not because they are dispensable, but rather because they represent a highly transient microglial state.

Our study further identifies IFITM3 as a novel marker of nascent microglial phagosomes, shedding light on the role of IFN-I signaling in microglial phagocytosis. IFITM3 is a potent interferon effector with roles in phagocytic initiation and endo-lysosomal trafficking during viral infection[100,101]. Interferon response genes, including IFITM3, can drive modifications of the lipid membrane that prevent viral fusion and promote lysosomal acidification[99,102]. IFN-I signaling has also been implicated in the maturation of autophagosomes[103]. Future investigations of how IFN-I and IFITM3 modulate microglial phagocytic capacity may yield mechanistic insight into this key function[104]. Many outstanding questions remain, including which cells release IFN-α/β, what signals drive microglia to engulf specific cells, and whether cells are eaten dead or alive[49,105–107]. Transcriptomic data suggests that microglia themselves could be a source of IFN-β[61]. One potential model is that exposure to damage associated molecular patterns (DAMPs) from stressed cells[48,108] triggers conserved responses adapted to detect nucleic acids[109–112], triggering an autocrine loop which enhances phagocytic efficiency via IFN- α/β release. In this model, physiological and self-contained engulfment events could become pathological if high IFN-I tone or abundant nucleic acids trigger a more widespread microglial response and lead to indiscriminate cell death and neuroinflammation.

Consistent with this proposed model, our data reveal the expansion of an IFN-I responsive microglial subset in the context of both sterile and non-sterile pathologies. While an IFN-I response is expected during neurotropic viral infection, as we observed in a SARS-CoV-2 model, the association of IFITM3+ microglia with virally infected neurons could prompt further inquiry into potential pathogenic mechanisms. Given emerging reports of neuropsychiatric sequelae following COVID-19 infection in humans[80,82], defining whether this microglial subset is present in human samples or in other animal models may be fruitful[113–115]. Furthermore, we identify and characterize a distinct IFITM3+ microglial subset *in situ* that associates with Aβ plaques in the 5xFAD model of Alzheimer's disease. This is consistent with multiple reports of IFN-I involvement in aging and Alzheimer's disease [67,76,89,90,116,117], and suggests potential roles for an IFN-I induced cell state in regulating Aβ deposition. Determining the mechanisms of microglial engulfment during cortical development and in pathology may enable therapeutics to target specific phases of the phagocytic cycle while preserving microglial homeostatic function.

Acknowledgements:

We are grateful to members of the Molofsky Lab and Dr. Aimee Kao for helpful comments on the manuscript, and thanks to Drs. Rafael Han and Nick Silva for assistance with tissue preparation. Thanks to the Chan-Zuckerberg Biohub for sequencing support. **Funding*:*** A.V.M is supported by the Pew Charitable Trusts, NIMH (R01MH119349 and DP2MH116507), and the Burroughs Welcome Fund. T.J.N. was supported by NIMH RF1MH121268. L.C.D. received support from the Matilda Edlund Scholarship and the Genentech Fellowship. P.T.N. is supported by a graduate research fellowship from the National Science Foundation (Grant #1650113). C.E. was supported by a gift from Marilyn Waldman. C.C. was supported by NIA RF1AG061874.

Author contributions:

Conceptualization: A.V.M and L.C.D.; Methodology, L.C.D., A.V.M, P.T.N., I.D.V., C.C.E., H. N-I., Y.X., B.R., C.C., R.A.; Investigation: L.C.D., P.T.N., I.D.V, S.E.T., C.C.E, E.W., B.R., Y.X., P.V.L.; Writing – Original Draft, L.C.D., P.T.N., C.C.E., and A.V.M.; Writing – Review & Editing, all co-authors; Funding Acquisition, A.V.M. Resources, A.V.M., C.C., R.A., Supervision, A.V.M., T.N., C.C., R.A., and I.D.V.

Declaration of interests: The authors declare no competing interests.

Data and materials availability: Supplement contains additional data. All data needed to evaluate the conclusions in the paper are present in the paper or the Supplementary Materials. Searchable database available at https://www.annamolofskylab.org/microglia-sequencing. RNA sequencing data is available through GEO at GSE173173. Code availability: R and Python code used to analyze single cell datasets is available on GitHub at https://github.com/lcdorman/IFNresponseCode.

Bibliography

1. Arguello, P. A. & Gogos, J. A. Genetic and cognitive windows into circuit mechanisms of psychiatric disease. *Trends in Neurosciences* **35**, 3–13 (2012).
2. Forrest, M. P., Parnell, E. & Penzes, P. Dendritic structural plasticity and neuropsychiatric disease. *Nature Reviews Neuroscience* **19**, 215–234 (2018).
3. Bitzenhofer, S. H., Pöpplau, J. A., Chini, M., Marquardt, A. & Hanganu-Opatz, I. L. A transient developmental increase in prefrontal activity alters network maturation and causes cognitive dysfunction in adult mice. *Neuron* (2021). doi:10.1016/j.neuron.2021.02.011
4. Medendorp, W. E. *et al.* Selective postnatal excitation of neocortical pyramidal neurons results in distinctive behavioral and circuit deficits in adulthood. *iScience* **24**, (2021).
5. Vainchtein, I. D. & Molofsky, A. V. Astrocytes and Microglia: In Sickness and in Health. *Trends in Neurosciences* (2020). doi:10.1016/j.tins.2020.01.003
6. Allen, N. J. & Lyons, D. A. Glia as architects of central nervous system formation and function. *Science* (2018). doi:10.1126/science.aat0473
7. Prinz, M., Jung, S. & Priller, J. Microglia Biology: One Century of Evolving Concepts. *Cell* (2019). doi:10.1016/j.cell.2019.08.053
8. Frost, J. L. & Schafer, D. P. Microglia: Architects of the Developing Nervous System. *Trends in Cell Biology* **26**, 587–597 (2016).
9. Hammond, T. R. *et al.* Single-Cell RNA Sequencing of Microglia throughout the Mouse Lifespan and in the Injured Brain Reveals Complex Cell-State Changes. *Immunity* (2019). doi:10.1016/j.immuni.2018.11.004
10. Li, Q. *et al.* Developmental Heterogeneity of Microglia and Brain Myeloid Cells Revealed by Deep Single-Cell RNA Sequencing. *Neuron* (2019). doi:10.1016/j.neuron.2018.12.006
11. Gosselin, D. *et al.* An environment-dependent transcriptional network specifies human microglia identity. *Science (80-.).* (2017). doi:10.1126/science.aal3222
12. Gosselin, D. *et al.* Environment drives selection and function of enhancers controlling tissue-specific macrophage identities. *Cell* (2014). doi:10.1016/j.cell.2014.11.023
13. Badimon, A. *et al.* Negative feedback control of neuronal activity by microglia. *Nature* (2020). doi:10.1038/s41586-020-2777-8
14. Lavin, Y. *et al.* Tissue-resident macrophage enhancer landscapes are shaped by the local microenvironment. *Cell* **159**, 1312–1326 (2014).
15. Chovatiya, R. & Medzhitov, R. Stress, inflammation, and defense of homeostasis. *Molecular Cell* **54**, 281–288 (2014).
16. Van Der Loos, H. & Woolsey, T. A. Somatosensory cortex: Structural alterations following early injury to sense organs. *Science (80-.).* (1973). doi:10.1126/science.179.4071.395
17. Sehara, K. *et al.* Whisker-Related Axonal Patterns and Plasticity of Layer 2/3 Neurons in the Mouse Barrel Cortex. *J. Neurosci.* (2010). doi:10.1523/jneurosci.6096-09.2010
18. Erzurumlu, R. S. & Gaspar, P. Development and critical period plasticity of the barrel cortex. *Eur. J. Neurosci.* (2012). doi:10.1111/j.1460-9568.2012.08075.x
19. Villani, A. *et al.* Clearance by Microglia Depends on Packaging of Phagosomes into a Unique Cellular Compartment. *Dev. Cell* (2019). doi:10.1016/j.devcel.2019.02.014

20. Sehara, K. & Kawasaki, H. Neuronal circuits with whisker-related patterns. *Mol. Neurobiol.* (2011). doi:10.1007/s12035-011-8170-8

21. Sugimoto, T. *et al.* Apoptotic cascade of neurons in the subcortical sensory relay nuclei following the neonatal infraorbital nerve transection. *Brain Res.* (1999). doi:10.1016/S0006-8993(99)01237-8

22. Baldi, A. *et al.* Deafferentation-induced apoptosis of neurons in thalamic somatosensory nuclei of the newborn rat: Critical period and rescue from cell death by peripherally applied neurotrophins. *Eur. J. Neurosci.* (2000). doi:10.1046/j.1460-9568.2000.00119.x

23. Woolsey, T. A. & Wann, J. R. Areal changes in mouse cortical barrels following vibrissal damage at different postnatal ages. *J. Comp. Neurol.* (1976). doi:10.1002/cne.901700105

24. Jeanmonod, D., Rice, F. L. & Van der Loos, H. Mouse somatosensory cortex: Alterations in the barrelfield following receptor injury at different early postnatal ages. *Neuroscience* (1981). doi:10.1016/0306-4522(81)90222-0

25. Stogsdill, J. A. *et al.* Astrocytic neuroligins control astrocyte morphogenesis and synaptogenesis. *Nature* **551**, 192–197 (2017).

26. Hoshiko, M., Arnoux, I., Avignone, E., Yamamoto, N. & Audinat, E. Deficiency of the Microglial Receptor CX3CR1 Impairs Postnatal Functional Development of Thalamocortical Synapses in the Barrel Cortex. *J. Neurosci.* (2012). doi:10.1523/jneurosci.1167-12.2012

27. Gunner, G. *et al.* Sensory lesioning induces microglial synapse elimination via ADAM10 and fractalkine signaling. *Nat. Neurosci.* (2019). doi:10.1038/s41593-019-0419-y

28. Rebsam, A., Seif, I. & Gaspar, P. Refinement of thalamocortical arbors and emergence of barrel domains in the primary somatosensory cortex: A study of normal and monoamine oxidase A knock-out mice. *J. Neurosci.* **22**, 8541–8552 (2002).

29. Rice, F. L., Gomez, C., Barstow, C., Burnet, A. & Sands, P. AComparative analysis of the development of the primary somatosensory cortex: Interspecies similarities during barrel and laminar development. *J. Comp. Neurol.* **236**, 477–495 (1985).

30. Adam, M., Potter, A. S. & Potter, S. S. Psychrophilic proteases dramatically reduce single-cell RNA-seq artifacts: A molecular atlas of kidney development. *Dev.* (2017). doi:10.1242/dev.151142

31. Mangin, J. M., Li, P., Scafidi, J. & Gallo, V. Experience-dependent regulation of NG2 progenitors in the developing barrel cortex. *Nat. Neurosci.* (2012). doi:10.1038/nn.3190

32. Singh, S. K. *et al.* Astrocytes Assemble Thalamocortical Synapses by Bridging NRX1α and NL1 via Hevin. *Cell* (2016). doi:10.1016/j.cell.2015.11.034

33. Ferris, H. A. *et al.* Loss of astrocyte cholesterol synthesis disrupts neuronal function and alters whole-body metabolism. *Proc. Natl. Acad. Sci. U. S. A.* (2017). doi:10.1073/pnas.1620506114

34. Valenza, M. *et al.* Disruption of astrocyte-neuron cholesterol cross talk affects neuronal function in Huntington's disease. *Cell Death Differ.* (2015). doi:10.1038/cdd.2014.162

35. Pfrieger, F. W. Role of cholesterol in synapse formation and function. *Biochimica et Biophysica Acta - Biomembranes* (2003). doi:10.1016/S0005-2736(03)00024-5

36. Mauch, D. H. *et al.* CNS synaptogenesis promoted by glia-derived cholesterol. *Science (80-.).* (2001). doi:10.1126/science.294.5545.1354

37. Tsai, H. I., Tsai, L. H., Chen, M. Y. & Chou, Y. C. Cholesterol deficiency perturbs actin signaling and glutamate homeostasis in hippocampal astrocytes. *Brain Res.* (2006). doi:10.1016/j.brainres.2006.05.081

38. Cybulska-Klosowicz, A., Zakrzewska, R., Pyza, E., Kossut, M. & Schachner, M. Reduced plasticity of cortical whisker representation in adult tenascin-C-deficient mice after vibrissectomy. *Eur. J. Neurosci.*

(2004). doi:10.1111/j.1460-9568.2004.03605.x

39. McRae, P. A., Rocco, M. M., Kelly, G., Brumberg, J. C. & Matthews, R. T. Sensory Deprivation Alters Aggrecan and Perineuronal Net Expression in the Mouse Barrel Cortex. *J. Neurosci.* (2007). doi:10.1523/jneurosci.5425-06.2007

40. Grau, S. *et al.* The role of human HtrA1 in arthritic disease. *J. Biol. Chem.* (2006). doi:10.1074/jbc.M500361200

41. Murwantoko *et al.* Binding of proteins to the PDZ domain proteolytic activity of HtrA1 serine protease. *Biochem. J.* (2004). doi:10.1042/BJ20040435

42. Tsuchiya, A. *et al.* Expression of mouse HtrA1 serine protease in normal bone and cartilage and its upregulation in joint cartilage damaged by experimental arthritis. *Bone* (2005). doi:10.1016/j.bone.2005.03.015

43. Lin, M. K. *et al.* HTRA1, an age-related macular degeneration protease, processes extracellular matrix proteins EFEMP1 and TSP1. *Aging Cell* (2018). doi:10.1111/acel.12710

44. Hong, S. *et al.* Complement and microglia mediate early synapse loss in Alzheimer mouse models. *Science (80-.).* (2016). doi:10.1126/science.aad8373

45. Schafer, D. P. *et al.* Microglia sculpt postnatal neural circuits in an activity and complement-dependent manner. *Neuron* (2012). doi:10.1016/j.neuron.2012.03.026

46. Miyamoto, A. *et al.* Microglia contact induces synapse formation in developing somatosensory cortex. *Nat. Commun.* (2016). doi:10.1038/ncomms12540

47. Nguyen, P. T. *et al.* Microglial Remodeling of the Extracellular Matrix Promotes Synapse Plasticity. *Cell* (2020). doi:10.1016/j.cell.2020.05.050

48. Boada-romero, E. *et al.* Mechanisms and physiology of the clearance of dead cells by efferocytosis. *Nat. Rev. Cell Biol.* (2020).

49. Fourgeaud, L. *et al.* TAM receptors regulate multiple features of microglial physiology. *Nature* **532**, 240–244 (2016).

50. Krasemann, S. *et al.* The TREM2-APOE Pathway Drives the Transcriptional Phenotype of Dysfunctional Microglia in Neurodegenerative Diseases. *Immunity* **47**, 566-581.e9 (2017).

51. Sierra, A. *et al.* Microglia shape adult hippocampal neurogenesis through apoptosis-coupled phagocytosis. *Cell Stem Cell* **7**, 483–495 (2010).

52. Blanquie, O. *et al.* Electrical activity controls area-specific expression of neuronal apoptosis in the mouse developing cerebral cortex. *Elife* (2017). doi:10.7554/eLife.27696

53. Haimon, Z. *et al.* Re-evaluating microglia expression profiles using RiboTag and cell isolation strategies. *Nat. Immunol.* (2018). doi:10.1038/s41590-018-0110-6

54. Bohlen, C. J., Bennett, F. C. & Bennett, M. L. Isolation and Culture of Microglia. *Curr. Protoc. Immunol.* (2019). doi:10.1002/cpim.70

55. Miltenyi, S., Müller, W., Weichel, W. & Radbruch, A. High gradient magnetic cell separation with MACS. *Cytometry* **11**, 231–238 (1990).

56. Marek, R., Caruso, M., Rostami, A., Grinspan, J. B. & Sarma, J. Das. Magnetic cell sorting: A fast and effective method of concurrent isolation of high purity viable astrocytes and microglia from neonatal mouse brain tissue. *J. Neurosci. Methods* **175**, 108–118 (2008).

57. Chris Bennett, F., Bennett, M. L., Gephart, H., Plowey, E. D. & Correspondence, B. A. B. A Combination of Ontogeny and CNS Environment Establishes Microglial Identity. *Neuron* **98**, 1170-

1183.e8 (2018).

58. McNab, F., Mayer-Barber, K., Sher, A., Wack, A. & O'Garra, A. Type I interferons in infectious disease. *Nature Reviews Immunology* **15**, 87–103 (2015).

59. Bergen, V., Lange, M., Peidli, S., Wolf, F. A. & Theis, F. J. Generalizing RNA velocity to transient cell states through dynamical modeling. *Nat. Biotechnol.* (2020). doi:10.1038/s41587-020-0591-3

60. Keren-Shaul, H. *et al.* A Unique Microglia Type Associated with Restricting Development of Alzheimer's Disease. *Cell* **169**, 1276-1290.e17 (2017).

61. Zhang, Y. *et al.* An RNA-sequencing transcriptome and splicing database of glia, neurons, and vascular cells of the cerebral cortex. *J. Neurosci.* (2014). doi:10.1523/JNEUROSCI.1860-14.2014

62. Li, T. *et al.* A splicing isoform of GPR56 mediates microglial synaptic refinement via phosphatidylserine binding. *EMBO J.* (2020). doi:10.15252/embj.2019104136

63. Scott-Hewitt, N. *et al.* Local externalization of phosphatidylserine mediates developmental synaptic pruning by microglia. *EMBO J.* (2020). doi:10.15252/embj.2020105380

64. Park, D. *et al.* BAI1 is an engulfment receptor for apoptotic cells upstream of the ELMO/Dock180/Rac module. *Nature* (2007). doi:10.1038/nature06329

65. Mazaheri, F. *et al.* Distinct roles for BAI1 and TIM-4 in the engulfment of dying neurons by microglia. *Nat. Commun.* (2014). doi:10.1038/ncomms5046

66. Grommes, C. *et al.* Regulation of microglial phagocytosis and inflammatory gene expression by Gas6 acting on the Axl/Mer family of tyrosine kinases. *J. NeuroImmune Pharmacol.* **3**, 130–140 (2008).

67. Hur, J. Y. *et al.* The innate immunity protein IFITM3 modulates γ-secretase in Alzheimer's disease. *Nature* (2020). doi:10.1038/s41586-020-2681-2

68. Bailey, C. C., Zhong, G., Huang, I. C. & Farzan, M. IFITM-family proteins: The cell's first line of antiviral defense. *Annu. Rev. Virol.* (2014). doi:10.1146/annurev-virology-031413-085537

69. Brass, A. L. *et al.* The IFITM Proteins Mediate Cellular Resistance to Influenza A H1N1 Virus, West Nile Virus, and Dengue Virus. *Cell* (2009). doi:10.1016/j.cell.2009.12.017

70. Lee, J. *et al.* IFITM3 functions as a PIP3 scaffold to amplify PI3K signalling in B cells. *Nature* (2020). doi:10.1038/s41586-020-2884-6

71. Uccellini, M. B. & García-Sastre, A. ISRE-Reporter Mouse Reveals High Basal and Induced Type I IFN Responses in Inflammatory Monocytes. *Cell Rep.* (2018). doi:10.1016/j.celrep.2018.11.030

72. Madisen, L. *et al.* A robust and high-throughput Cre reporting and characterization system for the whole mouse brain. *Nat. Neurosci.* (2010). doi:10.1038/nn.2467

73. Uribe-Querol, E. & Rosales, C. Phagocytosis: Our Current Understanding of a Universal Biological Process. *Frontiers in Immunology* (2020). doi:10.3389/fimmu.2020.01066

74. Chistiakov, D. A., Killingsworth, M. C., Myasoedova, V. A., Orekhov, A. N. & Bobryshev, Y. V. CD68/macrosialin: Not just a histochemical marker. *Lab. Investig.* (2017). doi:10.1038/labinvest.2016.116

75. Friedman, B. A. *et al.* Diverse Brain Myeloid Expression Profiles Reveal Distinct Microglial Activation States and Aspects of Alzheimer's Disease Not Evident in Mouse Models. *Cell Rep.* (2018). doi:10.1016/j.celrep.2017.12.066

76. Frigerio, C. S. *et al.* The Major Risk Factors for Alzheimer's Disease: Age, Sex, and Genes Modulate the Microglia Response to Aβ Plaques. *Cell Rep.* **27**, 1293–1306 (2019).

77. Zhang, Y. *et al.* Interferon-Induced Transmembrane Protein 3 Genetic Variant rs12252-C Associated

with Disease Severity in Coronavirus Disease 2019. *J. Infect. Dis.* (2020). doi:10.1093/infdis/jiaa224

78. Hachim, M. Y. *et al.* Interferon-Induced Transmembrane Protein (IFITM3) Is Upregulated Explicitly in SARS-CoV-2 Infected Lung Epithelial Cells. *Front. Immunol.* (2020). doi:10.3389/fimmu.2020.01372

79. Shi, G. *et al.* Opposing activities of IFITM proteins in SARS-CoV-2 infection. *EMBO J.* (2021). doi:10.15252/embj.2020106501

80. Song, E. *et al.* Neuroinvasion of SARS-CoV-2 in human and mouse brain. *J. Exp. Med.* (2021). doi:10.1084/JEM.20202135

81. Liotta, E. M. *et al.* Frequent neurologic manifestations and encephalopathy-associated morbidity in Covid-19 patients. *Ann. Clin. Transl. Neurol.* (2020). doi:10.1002/acn3.51210

82. Taquet, M., Luciano, S., Geddes, J. R. & Harrison, P. J. Bidirectional associations between COVID-19 and psychiatric disorder: retrospective cohort studies of 62 354 COVID-19 cases in the USA. *The Lancet Psychiatry* **8**, 130–140 (2021).

83. Moreau, G. B. *et al.* Evaluation of K18-hACE2 Mice as a Model of SARS-CoV-2 Infection. *Am. J. Trop. Med. Hyg.* (2020). doi:10.4269/ajtmh.20-0762

84. Winkler, E. S. *et al.* SARS-CoV-2 infection of human ACE2-transgenic mice causes severe lung inflammation and impaired function. *Nat. Immunol.* (2020). doi:10.1038/s41590-020-0778-2

85. Israelow, B. *et al.* Mouse model of SARS-CoV-2 reveals inflammatory role of type i interferon signaling. *J. Exp. Med.* (2020). doi:10.1084/JEM.20201241

86. McCray, P. B. *et al.* Lethal Infection of K18-hACE2 Mice Infected with Severe Acute Respiratory Syndrome Coronavirus. *J. Virol.* (2007). doi:10.1128/jvi.02012-06

87. Carossino, M. *et al.* Fatal neuroinvasion of SARS-CoV-2 in K18-hACE2 mice is partially dependent on hACE2 expression. *bioRxiv* (2021).

88. Kumari, P. *et al.* Neuroinvasion and Encephalitis Following Intranasal Inoculation of SARS-CoV-2 in K18-hACE2 Mice. *Viruses* (2021). doi:10.3390/v13010132

89. Baruch, K. *et al.* Aging-induced type I interferon response at the choroid plexus negatively affects brain function. *Science (80-.).* (2014). doi:10.1126/science.1252945

90. Roy, E. R. *et al.* Type I interferon response drives neuroinflammation and synapse loss in Alzheimer disease. *J. Clin. Invest.* (2020). doi:10.1172/JCI133737

91. Minter, M. R. *et al.* Deletion of the type-1 interferon receptor in APPSWE/PS1ΔE9 mice preserves cognitive function and alters glial phenotype. *Acta Neuropathol. Commun.* **4**, 72 (2016).

92. Orre, M. *et al.* Isolation of glia from Alzheimer's mice reveals inflammation anddysfunction. *Neurobiol. Aging* **35**, 2746–2760 (2014).

93. Oakley, H. *et al.* Intraneuronal β-amyloid aggregates, neurodegeneration, and neuron loss in transgenic mice with five familial Alzheimer's disease mutations: Potential factors in amyloid plaque formation. *J. Neurosci.* (2006). doi:10.1523/JNEUROSCI.1202-06.2006

94. Hansen, D. V., Hanson, J. E. & Sheng, M. Microglia in Alzheimer's disease. *Journal of Cell Biology* (2018). doi:10.1083/jcb.201709069

95. Liu, Z., Condello, C., Schain, A., Harb, R. & Grutzendler, J. CX3CR1 in microglia regulates brain amyloid deposition through selective protofibrillar amyloid-β phagocytosis. *J. Neurosci.* (2010). doi:10.1523/JNEUROSCI.4403-10.2010

96. Ivashkiv, L. B. & Donlin, L. T. Regulation of type i interferon responses. *Nature Reviews Immunology* (2014). doi:10.1038/nri3581

97. Brendecke, S. M. & Prinz, M. How type I interferons shape myeloid cell function in CNS autoimmunity. *J. Leukoc. Biol.* **92**, 479–488 (2012).

98. Kumaran Satyanarayanan, S. *et al.* IFN-β is a macrophage-derived effector cytokine facilitating the resolution of bacterial inflammation. *Nat. Commun.* **10**, 1–16 (2019).

99. Ranjbar, S., Haridas, V., Jasenosky, L. D., Falvo, J. V. & Goldfeld, A. E. A Role for IFITM Proteins in Restriction of Mycobacterium tuberculosis Infection. *Cell Rep.* (2015). doi:10.1016/j.celrep.2015.09.048

100. Wee, Y. S., Roundy, K. M., Weis, J. J. & Weis, J. H. Interferon-inducible transmembrane proteins of the innate immune response act as membrane organizers by influencing clathrin and v-ATPase localization and function. *Innate Immun.* (2012). doi:10.1177/1753425912443392

101. Spence, J. S. *et al.* IFITM3 directly engages and shuttles incoming virus particles to lysosomes. *Nat. Chem. Biol.* (2019). doi:10.1038/s41589-018-0213-2

102. Zhang, H., Zoued, A., Liu, X., Sit, B. & Waldora, M. K. Type i interferon remodels lysosome function and modifies intestinal epithelial defense. *Proc. Natl. Acad. Sci. U. S. A.* (2020). doi:10.1073/pnas.2010723117

103. Ejlerskov, P. *et al.* Lack of Neuronal IFN-β-IFNAR Causes Lewy Body- and Parkinson's Disease-like Dementia. *Cell* (2015). doi:10.1016/j.cell.2015.08.069

104. Galloway, D. A., Phillips, A. E. M., Owen, D. R. J. & Moore, C. S. Phagocytosis in the brain: Homeostasis and disease. *Frontiers in Immunology* (2019). doi:10.3389/fimmu.2019.00790

105. Brown, G. C. & Neher, J. J. Microglial phagocytosis of live neurons. *Nat. Rev. Neurosci.* **15**, 209–216 (2014).

106. Marín-Teva, J. L. *et al.* Microglia Promote the Death of Developing Purkinje Cells. *Neuron* **41**, 535–547 (2004).

107. Wakselman, S. *et al.* Developmental neuronal death in hippocampus requires the microglial CD11b integrin and DAP12 immunoreceptor. *J. Neurosci.* **28**, 8138–8143 (2008).

108. Chen, Q., Sun, L. & Chen, Z. J. Regulation and function of the cGAS-STING pathway of cytosolic DNA sensing. *Nature Immunology* (2016). doi:10.1038/ni.3558

109. Li, X. *et al.* Viral DNA Binding to NLRC3, an Inhibitory Nucleic Acid Sensor, Unleashes STING, a Cyclic Dinucleotide Receptor that Activates Type I Interferon. *Immunity* (2019). doi:10.1016/j.immuni.2019.02.009

110. Takaoka, A. & Yamada, T. Regulation of signaling mediated by nucleic acid sensors for innate interferon-mediated responses during viral infection. *International Immunology* (2019). doi:10.1093/intimm/dxz034

111. Wu, J. & Chen, Z. J. Innate immune sensing and signaling of cytosolic nucleic acids. *Annual Review of Immunology* (2014). doi:10.1146/annurev-immunol-032713-120156

112. Kawai, T. & Akira, S. Innate immune recognition of viral infection. *Nature Immunology* (2006). doi:10.1038/ni1303

113. Imai, M. *et al.* Syrian hamsters as a small animal model for SARS-CoV-2 infection and countermeasure development. *Proc. Natl. Acad. Sci. U. S. A.* **117**, 16587–16595 (2020).

114. Sia, S. F. *et al.* Pathogenesis and transmission of SARS-CoV-2 in golden hamsters. *Nature* **583**, 834–838 (2020).

115. Montagutelli, X. *et al.* The B1.351 and P.1 variants extend SARS-CoV-2 host range to mice. *bioRxiv* 2021.03.18.436013 (2021). doi:10.1101/2021.03.18.436013

116. Deczkowska, A. *et al.* Mef2C restrains microglial inflammatory response and is lost in brain ageing in an IFN-I-dependent manner. *Nat. Commun.* (2017). doi:10.1038/s41467-017-00769-0

117. Moore, Z., Mobilio, F., Walker, F. R., Taylor, J. M. & Crack, P. J. Abrogation of type-I interferon signalling alters the microglial response to Aβ1-42. *Sci. Rep.* **10**, 3153 (2020).

118. Galatro, T. F., Vainchtein, I. D., Brouwer, N., Boddeke, E. W. G. M. & Eggen, B. J. L. Isolation of microglia and immune infiltrates from mouse and primate central nervous system. in *Methods in Molecular Biology* (2017). doi:10.1007/978-1-4939-6786-5_23

119. Dobin, A. *et al.* STAR: Ultrafast universal RNA-seq aligner. *Bioinformatics* (2013). doi:10.1093/bioinformatics/bts635

120. Butler, A., Hoffman, P., Smibert, P., Papalexi, E. & Satija, R. Integrating single-cell transcriptomic data across different conditions, technologies, and species. *Nat. Biotechnol.* (2018). doi:10.1038/nbt.4096

121. Macosko, E. Z. *et al.* Highly Parallel Genome-wide Expression Profiling of Individual Cells Using Nanoliter Droplets. *Cell* (2015). doi:10.1016/j.cell.2015.05.002

122. Hoffman, G. E. & Schadt, E. E. variancePartition: Interpreting drivers of variation in complex gene expression studies. *BMC Bioinformatics* (2016). doi:10.1186/s12859-016-1323-z

123. Zhou, Y. *et al.* Metascape provides a biologist-oriented resource for the analysis of systems-level datasets. *Nat. Commun.* (2019). doi:10.1038/s41467-019-09234-6

124. Kowalczyk, M. S. *et al.* Single-cell RNA-seq reveals changes in cell cycle and differentiation programs upon aging of hematopoietic stem cells. *Genome Res.* (2015). doi:10.1101/gr.192237.115

125. La Manno, G. *et al.* RNA velocity of single cells. *Nature* (2018). doi:10.1038/s41586-018-0414-6

126. Jung, S. *et al.* Analysis of Fractalkine Receptor CX3CR1 Function by Targeted Deletion and Green Fluorescent Protein Reporter Gene Insertion. *Mol. Cell. Biol.* (2002). doi:10.1128/mcb.20.11.4106-4114.2000

127. Gong, S. *et al.* A gene expression atlas of the central nervous system based on bacterial artificial chromosomes. *Nature* (2003). doi:10.1038/nature02033

128. Prigge, J. R. *et al.* Type I IFNs Act upon Hematopoietic Progenitors To Protect and Maintain Hematopoiesis during Pneumocystis Lung Infection in Mice. *J. Immunol.* (2015). doi:10.4049/jimmunol.1501553

- CONTACT FOR REAGENT AND RESOURCE SHARING

Anna Molofsky, anna.molofsky@ucsf.edu

- EXPERIMENTAL MODELS AND SUBJECT DETAILS

Mice: All mouse strains were maintained in the University of California San Francisco specific pathogen–free animal facility, and all animal protocols were approved by and in accordance with the guidelines established by the Institutional Animal Care and Use Committee and Laboratory Animal Resource Center. Littermate controls were used for all experiments when feasible, and reporter mice were backcrossed >10 generations on a C57Bl/6 background (Cx3cr1-GFP) or Swiss-Webster (Aldh1l1-eGFP). The following mouse strains used are described in the table below and are as referenced in the text: Cx3cr1-GFP (JAX #00582); Aldh1l1-eGFP (Gensat); Ifnar1$^{-/-}$ (JAX #028288); Mx1-GFP (JAX #033219); Mx1-Cre (JAX #003556); Ai14 (JAX #007908); B6.Cg-Tg(K18-ACE2)2Prlmn/J (JAX #034860); B6SJL-Tg(APPSwFlLon,PSEN1*M146L*L286V)6799Vas/Mmjax (5xFAD, JAX #34840-Jax).

- METHOD DETAILS

Whisker lesions: Whisker ablations were performed under hypothermia-induced anesthesia and followed by topical application of lidocaine for pain management. Postnatal day two pups were anesthetized for 3 minutes in ice. An incision was made in the whisker pad along whisker rows B and D of one side of the face, and silver nitrate was used to cauterize the exposed whisker follicles in that row. After topical 2% lidocaine application the mice were reacclimated on a heating pad for at least 15 minutes before being returned to their home cage.

Immunohistochemistry and Confocal Microscopy: For all analyses of barrel cortex, mice were perfused transcardially with ~10 mL of ice-cold PBS followed by ~10 mL of 4% (weight/volume) paraformaldehyde diluted in PBS. For analyses of SARS-CoV-2 infected brains, animals were not perfused and were postfixed by immersion in 4% PFA for 72 hours prior to cryoprotection and sectioning. All other brains were post-fixed in 4% PFA for a minimum of 4 hours and then transferred to a 30% sucrose solution for a minimum of 24 hours. Tangential sections (flat mounts) of the barrel cortex were obtained by dissecting the cortex from the diencephalon following perfusion and flattening the dissected cortices ventral side down between two cryomolds. The sections were placed in between flat toothpicks laid horizontally in the cryomold, and the second mold was pressed down on top of the toothpicks to maintain uniform thickness. Brains were then flash frozen and sliced on a HM 440E freezing microtome (GMI Instruments) or embedded in OCT following 30% sucrose treatment and frozen at -80°C for a minimum of 1 day and then sectioned on a CryoStar NX70 Cryostat (Thermo Fisher) before being mounted on coverslips. Sections from control and deprived hemispheres of individual mice were mounted on the same slides for all experiments.

See resource table below for details of all antibodies used. Immunohistochemistry was performed as follows: brain sections were incubated in a blocking solution consisting of 5% normal goat serum (Thermo Fisher) and 0.1% Triton (Sigma-Aldrich) diluted in 1X PBS. Primary antibodies were diluted in 3% normal goat serum in 0.1% Triton and tissue was incubated on a shaker overnight at 4°C. Secondary antibodies were diluted in 3% normal goat serum and tissue was incubated on a shaker for 2 hours at room temperature. Brain sections were mounted on coverslips with ProLong Gold or Glass (Thermo Fisher) for all imaging. For staining with IFITM3 (Thermo Fisher #11714-1-AP), secondary antibody staining was done with goat anti-rabbit IgG, HRP-linked (Cell Signaling Technology #7074) and visualized with TSA Plus Cy3 detection system (Akoya Biosciences #NEL744001KT). For staining with SARS-CoV-2 Spike and N protein antibodies (GeneTex), an additional antigen retrieval step (70°C for 10min) was performed prior to blocking. Slides were imaged on an LSM 800 confocal microscope (Zeiss) using 20x, 40x, and 63x objectives. For analysis of phagocytic cups, slides were imaged on LSM 880 confocal microscope with AiryScan (Zeiss) using a 63x objective.

Fluorescent In Situ Hybridization (FISH): FISH experiments were performed using the RNAscope Multiplex Fluorescent Reagent Kit v1 assay (ACD Bio) as described by the manufacturer for fixed-frozen tissue, but eliminating the 60°C incubation prior to tissue dehydration. Brains were embedded in OCT following 30% sucrose treatment and frozen at -80°C for a minimum of 1 day prior to sectioning. Mouse *Htra1* RNAscope Probe (ACD Bio #423711-C2) was used to detect *Htra1* transcript. For immunohistochemical labeling with antibodies following the RNAscope assay, tissues were incubated with blocking and antibody solutions as described above immediately after RNAscope and washing four times, 5 minutes each. Confocal optical sections were imaged on a Zeiss 700 at 63x magnification through layer IV of flattened *en face* cortical sections of the barrel cortex. The Htra1 channel was thresholded to remove puncta smaller than 0.06 um^2 in area, and the puncta within a 10 um radius of each Aldh1l1-GFP+ astrocyte were counted. Three images each from at least two sections each of three separate mice were counted per condition.

Flow cytometry: For all flow cytometry experiments, animals were perfused transcardially with ice-cold D-PBS, mounted coronally in ice-cold isolation media (HBSS, 15 mM HEPES, 0.6% glucose, 1 mM EDTA pH 8.0) and 350 micrometer slices were prepared on a vibratome. A stereomicroscope was used to visually identify barrel regions; 1 mm^3 of tissue was collected per hemisphere. All data analysis was performed using FlowJo™ software.

For single cell sequencing of non-neuronal cells from the cortex, cells were isolated using a protocol modified from Adam et al 2017. Barrel cortex was enzymatically dissociated with psychrophilic proteases (PBS with 4 uL/mL DNAse (Sigma D4527-40KU), 5 mg/mL protease (Creative Enzymes NATE-0633, 175 ug/mL L-cysteine) incubated on ice for 20 minutes with gentle trituration every 5 minutes until tissue chunks were no longer visible. Cells were centrifuged at 300g for 5 minutes at 4°C. Pelleted cells were then washed with isolation medium and incubated in blocking solution consisting of anti-mouse CD16/32 antibody (Biolegend). Cells were sorted on a BD FACS Aria III and gated on forward/side scatter, live cells by Hoechst, CD11b-PE (eBioscience), and CD45-FITC (BioLegend) to identify, sort for, and enrich microglia. Microglia (CD11b+) and other cells were sorted into the blocking media described above and mixed at a ratio of 1/3 microglia: 2/3 non-microglial cells for 10x sequencing. Sorted cells were pelleted in an eppendorf tube at 300 g for 5 minutes at 4°C and then resuspended in blocking buffer consisting of 1% (weight/volume) RNase-free BSA and 1X PBS for downstream sequencing.

MACS Bead Isolation: For sorting microglia only for downstream RNA-sequencing, cells were isolated as described previously [118]. Briefly, barrel cortices dissected as described above were mechanically dissociated using a glass tissue homogenizer in isolation medium (HBSS, 15 mM HEPES, 0.6% glucose, 1 mM EDTA pH 8.0). Cells were filtered and then pelleted at 300 g for 10 minutes at 4°C before being resuspended in 22% Percoll (GE Healthcare) and centrifuged at 900 g for 20 minutes with acceleration set to 4 and deceleration set to 1 in order to remove cellular debris. Pelleted microglia were then resuspended in staining media (PBS, 0.5% BSA, 2 mM EDTA) and incubated with CD11b MACS beads (Miltenyi, 1:50) for 15 minutes at 4°C. The cells were washed with staining buffer, pelleted at 300 g for 5 minutes at 4°C, and reconstituted in 500 uL staining buffer. Microglia were isolated as described in the manual for MACS LS columns and collected in staining buffer without EDTA, pelleted at 300 g for 5 minutes at 4°C , counted on a hemocytometer, and 15,000-20,000 cells were diluted in 30 µL in a BSA-coated plate for 10x sequencing.

Single cell RNA-sequencing: Single cells were isolated as described above.
Pan-Glial isolation (Figure 1): Approximately 2,000 cells (v2, **Fig.**1-2) from each sample were loaded into each well of Chromium Chip A according to the manufacturer instructions and combined into droplets with barcoded beads using the Chromium controller. Libraries were prepared by the Gladstone Institutes Genomics Core following the instructions in the Chromium Single Cell 3' Reagent Kits version 2 user guide. The samples were sequenced to an average depth of 40,000-60,000 reads on an Illumina HiSeq 4000 sequencer.

Microglial single cell sequencing (Figure 2): Approximately 15,000 cells were loaded into each well of Chromium Chip B (v3, figure 3), libraries were prepared in-house as described in the 10x Manual, and sequenced on one lane of the NovaSeq S4 at the Chan-Zuckerberg BioHub.

Single cell data analysis: Sequenced samples were processed using the Cell Ranger 2.1 pipeline (built on the STAR aligner)[119] and aligned to the GRCm38 (mm10) mouse reference genome. Clustering and differential expression analysis were conducted using Seurat version 3.1.4. Data for figures 1 and 2 (total glial population) and figure 3 (microglia only) were prepared on different versions of the 10x Chromium platform and were therefore analyzed separately as detailed below. Sequencing scripts can be found at https://github.com/lcdorman/IFNresponseCode, and original data can be found on GEO at GSE173173.

	Whole Glial Isolation	Microglial Isolation
Number of cells (thresholded)	1777 cells; 357 astrocytes	12,330 microglia
Figures	1-2	3
Age	Postnatal day 7	Postnatal days 5 and 7
10x Chromium Kit	Chip A/V2	Chip B/V3
Feature thresholds	400-5000 genes/cell	2500-7500 genes/cell
% Mitochondrial RNA thresholds	0-5% mitochondrial RNA/cell	0-7.5% mitochondrial RNA/cell
Normalization	SCTransform	Log normalization/scale factor 10,000
Minimum % of cells expressing gene for diff. exp. Analysis	5%	10%
Clustering resolution (Seurat)	1.2 (clusters); 0.1 (celltypes); 0.6 (astrocytes)	0.5

Sorted cells were sequenced using the 10x Chromium kit. Following alignment in Cell Ranger as described above, counts were imported into R and analyzed using the Seurat package [120,121]. Cells outside of the thresholds listed in the table were excluded from downstream analysis. Cells were identified as "female" or "male" based on their expression of the gene *Xist*; any cells expressing at leaste one count of *Xist* were labelled female, while all others were labelled male. Counts were then normalized, regressing out percent mitochondrial RNA and total counts per cell. The top 6000 most variable genes were used to calculate 50 principal components, and the top 30 PCs were used for nearest neighbor, UMAP, and cluster calculations with the resolutions shown in the table. Individual celltypes were identified through calculation of marker genes using the Wilcox test for genes expressed in at least 50% of cells in the cluster and a natural log fold change of 1.2 or greater and adjusted p value less than 0.001.

For the cold protease experiment examining all non-neuronal cells (Fig.1) , the astrocyte cluster was isolated and reclustered based on the top astrocyte and microglial genes to remove 5 cells which showed high expression of microglial marker genes and separate the cells into three clusters. The remaining astrocytes were re-normalized and analyzed with the Variance Partition package [122] in R to determine the top 1,000 genes altered by condition. Differential expression analysis using Seurat's MAST function was then conducted using these genes between the control-enriched and deprived-enriched clusters. Volcano plots were generated using the EnhancedVolcano package in R, with gene labels chosen from the top differentially expressed genes. Cutoffs were set at natural log fold change greater than 0.25 (28% increase) and adjusted p-value smaller than 10^{-3}.

For the microglia only experiment (Fig. 2-on) , the microglial and macrophage clusters were isolated based on expression of Cx3cr1, Fcrls, P2y12, and low expression of non-microglial genes as shown in the heatmap. The filtered cells were re-normalized and analyzed with the Variance Partition package ([122] in R to determine the top genes determining sex, the first 8 of which were excluded from downstream analysis. The top 6000 most variable genes were used to recalculate PCs, UMAP, and clusters. Differential gene expression between clusters were calculated using the MAST test in Seurat. The heatmaps shown only include genes expressed by at least 50% of the cells in that cluster and with an adjusted p-value below 10^{-25}, sorted by highest log fold change. GO analysis was conducted using the Metascape webpage (www.metascape.org) [123]. Volcano plots were generated using the

EnhancedVolcano package in R, with gene labels chosen from the top differentially expressed genes. Cutoffs were set at natural log fold change greater than 0.2 (22% increase) and adjusted p-value smaller than 10^{-25}.

Cell cycle phase assignment: Cells were assigned to S phase, G1 phase, or G2/M phase (not distinguished) using a previously published dataset [124] and the CellCycleScoring function in Seurat.

"Eigengene" calculations: Subset-specific "Eigengenes" were calculated based on published differential gene expression signatures. All genes differentially expressed in a particular published subset with LFC > 1.5 and adj. $p < 10^{-8}$ were combined and an expression value for this eigengene was calculated using the PercentageFeatureSet function in Seurat, which calculates a percent expression per cell for any gene set. Ribosomal genes, which are expressed by all the clusters, were excluded from the analysis to avoid biasing the eigengene towards these highly expressed genes. Eigengene expression was validated by randomly sampling sets of 10 genes from the eigengene; every random sample showed the same gene expression pattern in the clustered data set as the full gene set, ensuring that a few genes were not biasing the entire eigengene.

RNA Velocity analysis: Spliced and unspliced transcript counts were calculated using Velocyto 0.17 and the velocyto run10x command with default settings. UMAP cell embeddings and annotation were exported from Seurat and used to plot all data shown. ScVelo 2.0.0 was run in Python and trajectories were calculated for all cells, then for each sample individually [59,125].

Bar plot creation: Bar plots were created using ggplot2 in R. Coding details are available on github (https://github.com/lcdorman/IFNresponseCode/blob/main/Code%20for%20paper/P5_P7%20Microglia/D_BarPlots.Rmd). A table was made of cells per cluster per sample. Cell numbers were normalized by sample by dividing each entry by the total number of cells for that sample and multiplying by 2,000. Percents per cluster were then calculated by dividing the normalized cell numbers by the total number of cells in that cluster and multiplying by 100. Statistics were calculated individually for each cluster using a Chi-Square test on the raw cell numbers per cluster and sample. Plots with multiple bars had an additional Bonferroni correction applied, which multiplies the p-value by the number of comparisons.

Atac-seq and microglial enrichment integration: "Microglial specificity" values were calculated using a published bulk sequencing dataset from developing mouse cortex [61]. FPKM values per gene in microglia were divided by the average FPKM for that gene in all other cell types to find a "Specificity score". A specificity score of 10 or higher was considered "Microglial specific" for the purposes of this study. An unpublished Atac-seq study of bulk microglia from adult mouse cortex was used to identify open chromatin promoter peaks for each gene. Peaks were called using Homer. Homer's "Peak Score" output was used to call peaks, which measures the position-adjusted number of reads identified for a particular promoter region. Only promoter peaks were considered, and if multiple promoter peaks were found for a single gene, only the one with the highest score was used. A promoter peak was only considered present if at least two of four samples had a peak score greater than 5. The minimum detectable peak had a value of 5, while the maximum detected was 5,000.

qPCR: To extract RNA from cells isolated by FACS, freshly sorted cells were pelleted at 500 g for 10 minutes at 4° and then resuspended in RLT Plus buffer (Qiagen). Cells were vortexed and frozen for at least one day at -80° before being thawed on ice and processed for RNA using an RNeasy Mini Kit (Qiagen). Purified mRNA was converted to cDNA with the High Capacity cDNA Reverse Transcription kit (Life Technologies) and amplified using either the Fast SYBR Green Master Mix (Thermo Fisher) or TaqMan Gene Expression Master Mix (Thermo Fisher) and a 7900HT Fast Real-Time PCR System (Applied Biosystems).

SARS-CoV-2 virus propagation and plaque assay: All SARS-CoV-2 cell culture and animals works were performed in the Biosafety level 3(BSL3). African green monkey kidney Vero-E6 cell line (ATCC#1586) and Calu-3 cells(ATCC# HTB-55) was obtained from American Type Culture Collection and maintained in Minimum Essential Medium (MEM, Gibco Invitrogen) supplemented with 10% fetal bovine serum (FBS, Gibco

Invitrogen), 1% Penicillin-Streptomycin-Glutamine (Gibco Invitrogen) at 37 °C in a humidified 5% CO2 incubator. A clinical isolate of SARS-CoV-2 from a UCSF patient was propagated in Vero E6 cells and Calu-3 cells. 80% Confluent monolayers of Vero E6 cells grown in 6-well plates were incubated with the serial dilutions of virus samples (250 ul/well) at 37 °C for 1 hour. Next, the cells were overlayed with 1% agarose (Invitrogen) prepared with MEM supplemented containing 2% fetal bovine serum(sigma), 1x penicillin/streptomycin/glutamine (100xPSG, Gibco). Three days later, the cells were fixed with 4% formaldehyde (PFA) for 2 hours, the overlay was discarded and samples were stained with crystal violet dye.

SARS-CoV-2 infection: 5-6 weeks old Hemizygous K18-hACE2 mice (The Jackson laboratory, https://www.jax.org/strain/034860, stock number: 034860, B6.Cg-Tg(K18-ACE2)2Prlmn/J) were anesthetized with isofluorane and inoculated with $6x10^4$ PFU of SARS-CoV-2 intranasally in a BSL3 facility. The mice were sacrificed at 3 and 6 days post- infection, and the brain was removed and fixed in 4% PFA for 72 hours before being sunk in 30% sucrose and embedded in OCT. 40 μm sections were cut on a cryostat and stained as described above with 2 minute antigen retrieval at 95 degrees. Antibodies used include the following: rabbit anti-SARS-CoV-2 Nucleocapsid(N) (GeneTex, GTX135361), mouse anti-SARS-CoV-2-spike(S), (GeneTex, GTX632604).

Microglia CD68 volume: Z-stacks were collected on an LSM 880 confocal microscope with AiryScan (Zeiss) on Superresolution mode and a 63x objective (NA 1.4). Laser power and gain were consistent across each image. AiryScan processing was performed in Zen software (Zeiss) at a setting of 6 (‘‘optimal’’ setting). Images were analyzed using Imaris software (Bitplane) by creating a 3D surface rendering of individual microglia, thresholded to ensure microglia processes were accurately reconstructed, and maintained consistent thereafter. Microglia rendering was used to mask and render the CD68 channel within each microglia. CD68 volume per microglia was then calculated as the total volume of masked CD68 volume within the masked GFP volume.

Microglia phagosome analyses: Phagosomes were identified as DAPI-enveloping structures that are distinct from the microglia nuclei. Unlike the microglia nuclear compartment, phagosomes lacked staining for Iba1 or GFP. Early phagosomes lacked CD68 and only partially enveloped a DAPI+ and non-pyknotic cell. For experiments in 5xFAD animals, phagosomes were identified as Iba1 deficient organelles at the terminal ends of microglia processes. Microglia with bubble morphology were identified by enlarged and rounded phagosomes that were larger than the microglia nucleus. These phagosomes contained DAPI+ nuclear material undergoing pyknosis or karyorrhexis, which were very sparsely distributed within the phagosome. In contrast, non-bubble phagosomes tightly enveloped engulfed nuclear material such that the DAPI signal saturated the phagosome area.

Z-stacks were acquired using an LSM 880 confocal microscope with AiryScan (Zeiss) on Superresolution mode and a 63x objective (NA 1.4, 0.04 um pixel size, 16-bit depth) and processed as described above. Phagosomes were analyzed in ImageJ and ROI’s were drawn around phagosomes using the Versatile Wand Tool plugin. The “tolerance” setting was manually adjusted to envelop the microglia phagosome surface and “connectedness” was set to 8-connected. An optical section was selected from the z-stack that represented the center of the phagosome and mean intensity, integrated density, and area were then recorded for each phagosome.

For analysis of phagosomes in Sars-CoV-2 infected mice, images were first binned by average IFITM3 MFI per microglia. The maximum microglial IFITM3 mean fluorescence intensity per image across all samples was called 100%. The lower bin represents images with 0-50% of the maximum expression, and the higher bin represents images with 50-100% of the maximum expression. Each microglia was then manually scored for presence or absence of a phagosome as described above. For experiments in 5xFAD mice determining microglia association with plaques, microglia that were within 10 μm of an Aβ plaque was considered plaque-associated.

- QUANTIFICATION AND STATISTICAL ANALYSIS

Graphpad Prism 8.3.0 was used for most statistical analyses of imaging data, and the Seurat package V3 in R was used for statistical analysis of single cell data. Statistical tests are as described in text and figure legends. Violin

plots were used for data with n > 20 to better visualize the distribution of individual data points. Single cell RNA-sequencing data was analyzed in R as described in the methods section above. Categorical data shown in bar plots (cluster-specific differences in cell numbers) were analyzed in R using a Chi-Square test on each cluster with Bonferroni's correction for multiple comparisons.

RESOURCE TABLE

REAGENT or RESOURCE		
Antibodies-immunostaining		
rabbit anti-dsRed 1:1000 (Clontech, 632496)		
chicken anti-GFP 1:1000 (Aves Labs, 1020)		
chicken anti-NeuN1:400 (Millipore, ABN91)		
rabbit anti-Iba1 1:1000 (Wako Chemicals, 019-19741)		
Mouse anti-Iba1 1:1000 (Wako Chemicals, 016-26721)		
Rat anti-P2ry12 1:100 (Biolegend, 848001)		
rabbit anti-P2y12 1:500 (David Julius Lab)		
rat anti-GFAP 1:1000 (Thermo Fisher, 13-0300)		
Rabbit anti-IFITM3 1:1:1000 (Thermo Fisher, 11714-1-AP)		
guinea pig anti-VGLUT2 1:2000 (Synaptic Systems, 135404)		
rat anti-CD68 1:500 (BioRad, MCA1957GA)		
Goat anti-rabbit IgG, HRP-linked (Cell Signaling Technology, 7074P2)		
Hoechst 33342 solution 1:5000 (Thermo Fisher, 62249) was used for nuclear labeling		
Mouse anti-Amyloid-Beta (4G8) 1:1000 (BioLegend, 800708)		
rabbit anti-SARS-CoV-2-N protein 1:1000 (GeneTex, GTX135361)		
mouse anti-SARS-CoV-2-Spike 1:1000 (GeneTex, GTX632604)		
Antibodies - flow cytometry		
TruStain rat anti-CD16/32 1:100 (BioLegend, 101319)		
APC rat anti-CD11b 1:100 (BioLegend, 101212)		
PE rat anti-CD11b 1:100 (eBioscience, 12-0112-81)		
FITC rat anti-CD45 1:100 (BioLegend, 103108)		
Critical Commercial Assays	Source	Cat #
RNAscope Multiplex Fluorescent Reagent Kit v1 assay, Mouse *Htra1* RNAscope Probe	Advanced Cell Diagnostics	320851, 423711-C2
TSA Plus Cyanine 3 and Fluorescein detection kits	Akoya Biosciences	NEL744001KT, NEL701A001KT
Chromium single cell gene expression platform, version 2 (Whole-glia RNAseq, Figures 1-2)	10x Genomics	Library and gel bead kit - V2, 120267 Chip A kit: 1000009
Chromium single cell gene expression platform, version 3 (Whole-glia RNAseq, Figures 1-2)	10x Genomics	Library and gel bead kit – V3, 1000075 Chip B kit: 1000074
Summary of Deposited Data		

Single cell RNA-sequencing of glial from postnatal day 7 barrel cortex after unilateral whisker follicle cauterization at postnatal day 2	Gene Expression Omnibus	*pending*
Single cell RNA-sequencing of microglia from postnatal day 5 and 7 barrel cortex after unilateral whisker follicle cauterization at postnatal day 2	Gene Expression Omnibus	*pending*
Experimental Models: Mouse strains		
Cx3cr1-GFP	JAX #00582	126
Aldh1l1-eGFP	GENSAT MGI:3843271	127
Ifnar1-/-	JAX #028288	128
Mx1-GFP	JAX #033219	71
Mx1-Cre	JAX #003556	[JAX]
Ai14	JAX #007908	72
B6.Cg-Tg(K18-ACE2)2Prlmn/J	JAX #034860	86
B6SJL-Tg(APPSwFlLon,PSEN1*M146L*L286V)6799Vas/Mmjax (5xFAD)	JAX #34840-Jax	93